

The VLA Survey of the Chandra Deep Field South.

II. Identification and host galaxy properties of submillijansky sources.

V. Mainieri^{1,2}, K.I. Kellermann³, E.B. Fomalont³, N. Miller^{3,4}, P. Padovani¹, P. Rosati¹, P. Shaver¹, J. Silverman^{2,5}, P. Tozzi⁶, J. Bergeron⁷, G. Hasinger², C. Norman^{4,8}, P. Popesso^{1,2}

ABSTRACT

We present the optical and infrared identifications of the 266 radio sources detected at 20 cm with the Very Large Array in the Chandra Deep Field South (Kellermann et al. 2008). Using deep i-band Advanced Camera for Surveys, R-band Wide Field Imager, K-band SOFI/NTT, K-band ISAAC/VLT and Spitzer imaging data, we are able to find reliable counterparts for 254 ($\sim 95\%$) VLA sources. Twelve radio sources remain unidentified and three of them are “empty fields”. Using literature and our own data we are able to assign redshifts to 186 ($\sim 70\%$) radio sources: 108 are spectroscopic redshifts and 78 reliable photometric redshifts. Based on the rest frame colors and morphological distributions of the host galaxies we find evidences for a change in the submillijansky radio source population: a) above ≈ 0.08 mJy early-type galaxies are dominating; b) at flux densities below ≈ 0.08 mJy, starburst galaxies become dominant.

Subject headings: Cosmology: observations - Galaxies: active-starburst – Radio continuum: galaxies

¹ESO, Karl-Schwarschild-Strasse 2, D-85748 Garching, Germany

²Max Planck Institut für extraterrestrische Physik, Giessenbachstrasse 1, D-85748 Garching, Germany

³National Radio Astronomy Observatory, 520 Edgemont Road, Charlottesville, VA 22903-2475, U.S.A.

⁴Department of Physics and Astronomy, Johns Hopkins University, Baltimore, MD 21210, U.S.A.

⁵Institute of Astronomy, Department of Physics, Eidgenössische Technische Hochschule, ETH Zurich, CH8093, Switzerland

⁶INAF Osservatorio Astronomico di Trieste, via G.B. Tiepolo 11, I-34131, Trieste, Italy

⁷Institut d’Astrophysique de Paris, 98bis Boulevard, F-75014 Paris, France

⁸Space Telescope Science Institute, 3700 S. Martin Drive, Baltimore, MD 21210, U.S.A.

1. Introduction

Deep radio surveys have shown that there is an upturn in the differential radio source counts below $\sim 1mJy$ that cannot be reproduced by evolutionary models of the millijansky radio populations (e.g Condon & Mitchell 1984; Windhorst et al. 1985; Ciliegi et al. 1999; Gruppioni et al. 1999; Richards et al. 2000; Seymour et al. 2004; etc.). Dedicated follow-up spectroscopic programs of many of these deep radio surveys (e.g. Thuan et al. 1987; Prandoni et al. 2001; Afonso et al. 2005) have shown that the submillijansky radio sources are mainly identified with faint blue galaxies with disturbed morphologies indicative of interactions and merging activity. However, due to the faint magnitudes of a large fraction of these submillijansky sources, all these works are based on a small percentages of identifications. Interestingly, Gruppioni et al. (1999) has shown that even at submillijansky level a large fraction of the radio sources are identified with early-type galaxies once the spectroscopic follow-up reaches fainter magnitude limit.

The aim of this paper is to identify the radio sources in one of the best studied region of the sky, the Chandra Deep Field South (CDF-S) and to study the properties of their host galaxies down to faint radio flux densities. The CDF-S area has been imaged with the Very Large Array (VLA) down to $8.5 \mu Jy$ rms near the field center and $3.5''$ resolution at both 1.4 and 5 GHz. The radio catalogue include 266 sources. Details on the reduction process and the overall VLA data are reported in Kellermann et al. (2008), Paper I. The CDF-S region is the area of the sky with the most extensive multi-wavelength observations available, covering an impressively wide range of wavelength. All of NASA’s existing Great Observatories (HST, Chandra and Spitzer), ESA’s XMM-Newton and the Very Large Telescope at ESO have devoted hundreds of hours each to obtain state-of-the-art sensitivities in this field. The large amount of ancillary data made the VLA survey in the CDF-S extremely valuable to understand better the properties of the submillijansky radio population. At the same time the radio data can help resolving uncertainties on the identification or the nature of sources selected at other wavelengths.

The paper is structured as follows: in Section 2 we provide a general description of the ancillary data used in the identification process; in Section 3 the identification methodology is described; we present in Section 4 the identification catalogue; in Section 5 we report on some particular sources with problematic identification; Section 6 describes the redshift distribution of the VLA sources; Section 7 is devoted to the discussion of the properties of the host galaxies and finally we summarize our conclusions in Section 8.

We use in this paper magnitudes in the AB system, if not otherwise stated, and we assume a cosmology with $H_0 = 70 \text{ km s}^{-1} \text{ Mpc}^{-1}$, $\Omega_M = 0.3$ and $\Omega_\Lambda = 0.7$.

2. Optical and NIR data

While we refer the reader to Kellermann et al. (2008) for an overview of the multi-wavelength coverage of the CDF-S area, in this section we describe the datasets used for the identification of the radio sources.

In the optical band, we used data obtained respectively with the Advanced Camera for Surveys (ACS) on board of HST and the Wide Field Imager (WFI) installed at the 2.2m telescope in La Silla. A central area of 160 arcmin² (dashed line in Fig. 1) has been covered by ACS in four different filters: F435W (b), F606W (v), F775W (i) and F850LP (z). These data have been taken as part of 'The Great Observatories Origins Deep Survey' (Dickinson et al. 2003; Giavalisco et al. 2004) down to the following limiting magnitudes (5σ in a 1 sq. arcsec area): 26.7, 26.7, 25.9, 25.6. For our identification purposes we used the F775W (i) band catalogue, which is publicly available on the GOODS web-site¹. For the outer region of our VLA survey not overlapping with the GOODS-ACS area, we used the WFI R (652 nm) band images from the ESO Imaging Survey (EIS)². These data cover the whole VLA survey down to a limiting magnitude of 25.5 (AB, 5σ in 2 arcsec aperture).

In the NIR, we used the ISAAC/VLT K_S (2162 nm) data from the GOODS survey on a central area of ~ 131 arcmin² (continuous line in Fig. 1). The mean limiting magnitude of this observation is 24.7 (AB, 5σ in 1 arcsec apertures; Retzlaff et al. in preparation)³. Finally, we have used shallower imaging in the K_S band obtained with SOFI/NTT (21.4, AB, 5σ in 2 arcsec aperture; Olsen et al. 2006) which covers the whole VLA survey.

The offsets between the radio catalogue and each one of the optical/NIR catalogs has been computed using a sample of point-like radio sources with $S/N > 5$ associated to a point-like counterpart. In Fig. 2 we show the $\Delta RA = RA(\text{radio}) - RA(\text{optical/NIR})$ and $\Delta Dec = Dec(\text{radio}) - Dec(\text{optical/NIR})$ in the case of the WFI-R catalogue (left panel) and SOFI-Ks catalogue (right panel). We found mean offsets of $\langle \Delta RA \rangle = 0.20 \pm 0.06$ arcsec and $\langle \Delta Dec \rangle = 0.09 \pm 0.08$ arcsec for WFI-R, and $\langle \Delta RA \rangle = 0.13 \pm 0.04$ arcsec and $\langle \Delta Dec \rangle = 0.12 \pm 0.06$ arcsec for SOFI-Ks. Similar offsets have been computed for the other catalogs (see Table 1). Before proceeding in the identification process, we correct for these mean offsets each one of the optical/NIR catalogs, in order to have radio and optical/NIR positions in the same reference frame.

¹<http://www.stsci.edu/science/goods/>

²<http://www.eso.org/science/goods/imaging/products.html>

³http://archive.eso.org/archive/adp/GOODS/ISAAC_imaging_v2.0/index.html

3. Identification methodology

Due to the faintness of both radio and optical samples, we could have more than one candidate counterpart for a single radio source. Therefore we used the likelihood ratio technique which provides a reliability measure of an identification as a function of the distance of the counterpart and of its magnitude. This technique has been first used in this context by Richter (1975) and since by de Ruiter et al. (1977), Prestage et al. (1983), Windhorst et al. (1984), Wolstencroft et al. (1986), Sutherland & Saunders (1992), Ciliegi et al. (2003), Ciliegi et al. (2005), Brusa et al. (2005) and Brusa et al. (2007).

The likelihood ratio (LR) is the probability that a given source with offset r and measured magnitude m is the true counterpart, relative to the probability that the same object is a chance background source:

$$LR = \frac{q(m)f(r)}{n(m)} \quad (1)$$

where $q(m)$ is the expected probability distribution as a function of magnitude of the true counterparts, $f(r)$ is the probability distribution of the positional errors, and $n(m)$ is the surface density as a function of magnitude of background objects. We refer the reader to Ciliegi et al. (2003) for a detailed discussion on the procedure to calculate $q(m)$, $f(r)$ and $n(m)$. In particular, to derive an estimate of $q(m)$ we adopt a radius of 2 arcsec to maximize the over-density due to the presence of the optical/NIR counterparts (we expect that the majority of the true optical/NIR counterparts are inside a 2 arcsec circle around the radio position). Inside $f(r)$ both the radio and optical/NIR positional uncertainties are included. For the optical/NIR positional error we assume 0.05 arcsec while for the radio uncertainties we use the values reported in Table 1 of Kellermann et al. (2008).

In Fig. 3 we show the distribution of the different components of Eq. (1) for the WFI-R catalogue, specifically the magnitude distribution of background objects that we expect to have in the area where the search for counterparts is performed (dashed histogram). This distribution is obtained multiplying the surface density as a function of magnitude of background objects, $n(m)$, times the area of a circle of 2 arcsec radius times the number of radio sources. The black filled histogram is the magnitude distribution of possible counterparts found in circles of 2 arcsec radius around the radio sources and the grey hatched histogram represents the expected magnitude distribution for the true optical counterparts once the background objects have been removed. We choose a threshold value for the likelihood ratio of $LR_{\text{th}} = 0.2$ and we will consider objects below this value as spurious counterparts. We find that this value is a good compromise between having a low enough threshold to avoid missing many real identifications and large enough to have few spurious ones.

Apart from a LR value for each possible counterparts, we would like to have a measure of the reliability of a particular source to be the true counterpart. Sutherland & Saunders (1992)

first pointed out that the presence or absence of other candidate counterparts for a single radio source provides *additional information* to that contained in LR and they developed a self-consistent formula for the reliability R_j of an object j to be the true counterpart:

$$R_j = \frac{LR_j}{\sum_i LR_i + (1 - Q)} \quad (2)$$

where i runs over the set of all candidate counterparts for that particular radio source, and $Q = \int_{-\infty}^{m_{lim}} q(m) dm$ is the probability that the counterpart of the source is above the magnitude limit of the optical/NIR catalogue. We choose $Q = 0.8$ corresponding to the ratio of the expected number of identification, the integral of $q(m)$, and the total number of radio sources. We note that for values of Q in the range 0.5-1.0 there is no significant difference in the result of the identification process.

To summarize, we adopt the following criterium to choose the most likely counterpart for a radio source: a) if only one candidate counterpart with $LR > LR_{th}$ is available, this will be chosen; b) if there are several candidate counterparts with $LR > LR_{th}$, we will choose the one with the highest reliability (R_j) value. We will call “empty field” a radio source with no candidate counterpart within a distance of 10 arcsec from the radio position.

4. Identifications

We use four different catalogs (ACS-i, WFI-R, ISAAC-Ks and SOFI-Ks) and the procedure outlined in the previous section to identify the counterparts of the VLA sources in the CDF-S area. In this section, we first report on the identification success rate for each one of these datasets and finally summarize the overall results of the identification process.

We find reliable counterparts for 67 ($\sim 85\%$) of the 79 radio sources inside the area covered by ACS/GOODS. The expected number of true counterparts, given by the sum of the reliability (R) values for all sources with $LR > LR_{th}$, is ~ 66.7 , therefore we expect that less than one of the optical counterparts found from the ACS/GOODS catalogue could be spurious. We are not able to assign an optical counterpart to twelve radio sources of which four have a possible counterpart with $LR < LR_{th}$ while eight appear like “empty-field” in the ACS images. The WFI-R catalogue covers the all VLA image and we find reliable counterpart for 230 ($\sim 86\%$) of the 266 radio sources. Of these we expect a maximum of three spurious identifications. The number of unidentified sources is 36, twelve of which are “empty-field”. From the NIR catalogs, we are able to identify 56 (92%) of the 61 radio sources with ISAAC-Ks imaging and we expect that less than one of these should be spurious. The shallower SOFI-Ks catalogue cover the all VLA area and it provides reliable counterparts for 190 (71%) of the 266 radio sources of which likely no more than six could be spurious. The surface

density of NIR sources is lower compared to that of optical objects therefore we expect less spurious identifications due to background sources: one for ISAAC and two for SOFI. Using the NIR catalogs we are able to assign reliable counterpart to 18 radio sources that were not identified in the optical.

Finally, to maximize the number of radio sources identified, we consider two additional datasets. The GEMS (Galaxy Evolution from Morphologies and SEDs) program Rix et al. (2004) has imaged in two filters, F606W(v) and F850LP(z), with ACS the whole area covered by our radio survey. Using this data we are able to find reliable counterparts for five radio sources previously unidentified (ID= 19, 46, 78, 176, 213). We also use the Spitzer (3.6, 4.5, 5.8, 8.5, 24 micron) images obtained as part of GOODS and the Spitzer/MIPS (24 and 70 micron) observations performed as part of FIDEL⁴ (PI Mark Dickinson): from these mid-IR images we find reliable counterparts for five additional radio sources (ID = 70, 87, 100, 105, 216). Summarizing, from the optical, NIR catalogs, and including the additional identifications from GEMS and Spitzer data, we find reliable counterparts for 254 ($\sim 95\%$) of the 266 radio sources. The number of spurious identifications due to background objects is expected to be lower than eight. Twelve radio sources remain unidentified: three of them are '*empty fields*' while the remaining nine have possible counterparts but with $LR < LR_{th}$. We summarize the output of the likelihood ratio process in Table 2. The left panel of Fig. 4 shows the cumulative distribution for the radio to optical/NIR distances: 90% of the counterparts are found inside a circle of 1.3'' radius and the maximum distance of a counterparts is 2.5''. We note that there are 20 radio sources with an optical counterpart at more than 1.3'' distance, eleven of these are with extended radio images and this can explain the large distance between the radio and the optical/NIR position. The other nine counterparts of radio sources that are unresolved, generally have low reliability values. In the right panel of Fig. 4 we show the distribution of the reliability parameter (R) for the 254 counterparts: 90% of them have $R > 0.83$.

We present in Table 3 the catalogue⁵ for the optical/NIR identification of the radio sources in the VLA/CDF-S area. The catalogue is organized as follows:

- Column 1 The radio source number used in this paper (see also Kellermann et al. 2008).
- Column 2-3 The Right Ascension and Declination (J2000) of the radio source (see also

⁴<http://www.noao.edu/noao/fidel/>

⁵A machine readable format of Table 3 is available in the electronic version of the paper.

Kellermann et al. 2008).

- Column 4-5 The Right Ascension and Declination (J2000) of the primary counterpart. The positional error is 0.05 arcsec.
- Column 6 The separation, in arcsec, between the radio source and its counterpart
- Column 7 The likelihood ratio (LR) as defined in Sec. 3
- Column 8 The reliability parameter (R) as defined in Sec. 3
- Column 9 The catalogue from which the counterpart was selected: *ACS-i* (i band catalogue from ACS/GOODS), *WFI-R* (R band catalogue from WFI), *ISAAC-K* (K band catalogue from ISAAC), *SOFI-K* (K band catalogue from SOFI), *GEMS* (z band catalogue from ACS/GEMS), *SPITZER* (IRAC and MIPS images)
- Column 10 The R band magnitude (AB)
- Column 11 The K band magnitude (AB)
- Column 12 The spectroscopic redshift of the counterpart
- Column 13 Quality flag for the spectroscopic redshifts: '2' secure redshift (multiple spectral features), '1' tentative redshift (e.g. based on a single emission line)
- Column 14 The photometric redshift of the counterpart

For some radio source we find more than one possible counterpart with $LR > LR_{\text{th}}$. We call primary the counterpart with the highest reliability value (Table 3) and secondary the remaining ones. Table 4 contains the properties of these secondary counterparts.

For each one of the 266 radio sources we have produced an optical cutout (see Fig. 5) using the *ACS-i* GOODS images, the *ACS-z* data from GEMS or finally, for those radio sources not covered by ACS, the WFI-R mosaic. The default size of the cutouts is 10×10 arcsec. We indicate the radio position (red cross), the primary counterpart (green square), and secondary counterpart (blue circle).

As already mentioned, for 18 radio sources unidentified in the optical, a reliable counterpart is found in the NIR bands. Optical and K band cutouts for these objects are shown in Fig. 6.

Five radio sources are correctly identified only from the Spitzer observations in the CDF-S

region. We show in Fig. 7 their optical and Spitzer cutouts. The details of these five sources are the following:

RID 70 - J033159.82-274540.3 The most likely counterpart becomes visible only at 4.5 μm . This radio source is also in the ATCA 1.4GHz survey (Afonso et al. 2006), ATCDFS J033159.86-274541.3, and the distance between the two radio coordinates is ~ 1 arcsec. This source was unidentified in Afonso et al. (2006) since they limited the search for counterparts to the optical bands.

RID 87 - J033209.90-275015.7 The counterpart is clearly visible in all the four IRAC bands.

RID 100 - J033213.31-273934.1 The counterpart is visible only in the 4.5 μm Spitzer image.

RID 105 - J033215.39-275037.5 The counterpart of this radio source become visible only in the Spitzer bands. This object is also detected with Chandra (XID= 587) and it was identified in Giacconi et al. (2002) with a R= 21.0 galaxy located at ~ 1.8 arcsec south-west of the X-ray position. We believe that this X-ray source has the same counterpart as the one chosen for the the radio source. The spectroscopic redshift for XID= 587 of $z= 0.246$ reported by Szokoly et al. (2004) belongs to the old counterpart, while for the newly proposed counterpart we currently have only a photometric redshift estimate of 1.80 ± 0.08 (Grazian et al. 2006).

RID 216 - J033303.30-275328.0 The most likely counterpart is visible only in the 3.6 μm Spitzer image. .

We show in Fig. 8 the R magnitude distribution for the primary counterparts (the total histogram). We highlight sources with a spectroscopic redshift (black shading) and the ones with a photometric redshift (grey shading). It is clear from this plot how the ability to obtain a redshift for the optical counterparts decreases going to fainter magnitudes: $\sim 88\%$ of the objects with $R_{AB} < 24$ have a redshift (spectroscopic or photometric) while this fraction decreases to $\sim 30\%$ for sources with $R_{AB} > 24$.

5. Notes on particular sources

Some of the identifications presented need further discussion due to a complex appearance either in the optical/NIR or in the radio band. Cutouts of each of these source are shown in Fig. 9. The component letters in this section refer to radio source components as given in Table 1 of Kellermann et al. (2008).

RID 7 - J033115.06-275518.4 This complex multi-component radio source is identified with an $R \sim 21$ optical/NIR galaxy coincident with component B.

RID 18 - J033127.23-274247.6 A possible blending of two sources, the counterpart, a $R = 24$ galaxy, coincident with the component A.

RID 23 - J033130.05-273814.2 Assuming that the central component is the core of a double lobed objects, we tentatively identified the radio source with a faint ($R \approx 26$) optical source.

RID 30 - J033138.56-273808.8 The faint radio source ($S_{1.4} = 175 \mu Jy$) is extended towards the faint galaxy to the south-west. It is likely a blend of two faint sources with the south-west one identified with the counterpart we have given in our catalogue.

RID 50 - J033150.35-274119.1 The counterpart ($R = 23.9$) listed in Table 3 is close to the peak of the radio emission and is relatively red ($K_S = 20.6$), while an extension of the radio emission points south to a ~ 3 arcsec distant spiral galaxy ($R = 21.5$). The photometric redshift from COMBO-17 reported in Table 3 could be affected by the contamination in the optical bands of a nearby (≈ 1.3 arcsec) source.

RID 60 - J033154.90-275340.5 Probably the blend of two radio sources. Currently, in Table 3 is listed the possible counterparts, $R = 24.5$, for one of the two sources; the other blended radio source could be identified with a $R = 21.3$ galaxy with an offset of ~ 3 arcsec from the radio centroid.

RID 113 - J033219.17-275407.7 This is a powerful extended double lobed radio source (FR II). We choose as the most likely counterpart the secondary according to our method based on LR (blue triangle in the inset of the figure). The same counterpart was also chosen for the X-ray source 249 (Giacconi et al. 2002). Higher resolution is needed to be certain of the optical counterpart. Another X-ray source from Giacconi et al. (2002), XID= 527 is coincident with the bright peak on the southwest radio lobe (component C); not surprisingly this X-ray source was unidentified.

RID 122 - J033222.49-274805.4 This radio source is identified with a $K = 22.8$ galaxy located at ~ 0.5 arcsec from the VLA position. This counterpart is not visible in the optical bands but is brighter in the NIR and in all the four IRAC/Spitzer bands. This object is also detected with Chandra (XID= 570 from Giacconi et al. 2002) and it was identified with a $R = 24.6$ galaxy located ~ 1.2 arcsec north-east of the X-ray position. We propose that this X-ray sources is identified with the same counterpart of the radio source. This radio source is also part of the ATCA 1.4 GHz catalogue presented by Afonso et al. (2006), ATCDFS J033222.36-274807.3, and the distance between the two radio positions is ~ 2.6 arcsec. In their catalogue, this source remains unidentified, we note that our K band counterpart candidate is ~ 4 arcsec from the Afonso et al. (2006) radio position.

RID 140 - J033228.83-274356.4 This source is identified with an $I \sim 18.3$ galaxy 0.6 arcsec from the central radio component (RID 140A). This identification is also supported by

an X-ray detection (XID=103 from Giacconi et al. 2002). We note that Afonso et al. (2006) reported a radio source, ATCFDS J033228.71-274402.3, ~ 7 arcsec away from our radio position. This ATCA source remained unidentified in their catalogue, and we believe this was due to the less accurate position provided by the ATCA survey compared to our. Finally, another X-ray detection, XID=630 from Giacconi et al. (2002), was tentatively identified with a $R \approx 23$ galaxy, we suggest that is instead be associated with the south component of this radio jet (B).

RID 169 - J033239.47-275301.3. This radio source is associated with a pair of interacting galaxies. One of the galaxies has a spectroscopic redshifts of $z=0.686$ (Vanzella et al. 2005) while the other as a photometric redshifts estimate of $z_{\text{phot}} = 0.65 \pm 0.01$ from COMBO-17.

RID 176 - J033242.57-273816.4 A double lobe radio galaxy. The likely core is clearly visible at $4.5 \mu m$ with Spitzer.

RID 178 - J033244.20-275142.1 This radio source is probably the blend of two objects (A and B) that correspond to a couple of interacting galaxies at $z=0.279$ (Szokoly et al. 2004). The counterpart of 178A has high excitation emission lines from the optical spectrum typical of an AGN and is also an X-ray source (XID= 98; Giacconi et al. 2002).

RID 186 - J033246.83-274215.1 This $S_{20cm} \sim 122 \mu Jy$ radio source is offsetted from the center of a bright ($R \approx 16.3$) galaxy. An X-ray source (XID= 84; Giacconi et al. 2002) is coincident with the centroid of the galaxy.

RID 207 - J033257.08-280209.7 The optical counterpart of this bright extended double radio source coincides also with an X-ray detection (XID= 508; Lehmer et al. 2005). The galaxy could be the central CD galaxy of a group/cluster of galaxies at $z= 0.664 \pm 0.001$ (photometric redshift from COMBO-17) and several arc-like structures can be clearly seen in the ACS image (see inset in the cutout).

RID 215 - J033303.22-275306.1 The radio emission is coming from two interacting galaxies with consistent estimates of the photometric redshifts from COMBO-17, $z_{\text{phot}} = 0.73 \pm 0.10$ and $z_{\text{phot}} = 0.82 \pm 0.06$.

RID 244-245-248 These three radio sources could be one single sources with two lobes. We note that RID=248 has a possible counterpart (mag $R \sim 24$, distance ~ 0.8 arcsec) with $LR > LR_{\text{th}}$ which is not consistent with it being a lobe of the radio source, but it could be the base of a jet which includes RID 244 and 245.

We are not able to find any counterpart for the following radio sources (see Fig. 10):

RID 97 - J033213.09-274350.7 This bright radio source ($S_{20cm} = 1.42$ mJy) remains unidentified although is inside the GOODS area and therefore covered by deep ACS, ISAAC and Spitzer imaging. This radio source corresponds to ATCFDS J033213.08-274351.0 of

Afonso et al. (2006). We considered the possibility that RID 92 and RID 97 might be lobes of a double radio galaxy. RID 92 lies 38 arcsec away. However, RID 92 appears to be firmly identified with an R \sim 22 galaxy, 0.2 arcsec from the radio position and coincide with an X-ray source, so this interpretation is unlikely. RID 97 is slightly resolved, but about half of the flux density appears to be in an unresolved component, suggesting that it is an isolated source. However, we cannot exclude the possibility, that RID 97 is part of RID 92, although there is no evidence of a connection between the two sources.

RID 155 - J033235.02-275455.2 This source ($S_{20cm} = 0.25$ mJy) remains unidentified although is inside the GOODS area and therefore covered by deep ACS, ISAAC and Spitzer imaging.

RID 202 - J033252.54-275942.9 This radio source ($S_{20cm} = 0.1$ mJy) remains unidentified. It is outside the GOODS area therefore is not covered by the deep IR imaging by ISAAC and Spitzer.

6. Redshift distribution

We have compared the primary counterparts found in Sec. 4 with the spectroscopic catalogs available in the CDF-S area. A total of 108 ($\sim 41\%$) radio sources have a spectroscopic redshift. Thirty-six redshifts are provided by the follow-up campaign of the X-ray sources in the CDF-S (Szokoly et al. 2004), seven from the FORS-2/GOODS program (Vanzella et al. 2005, 2006, 2008), 25 from the VIMOS/GOODS program (Popesso et al. 2008), six from the VVDS survey (Le Fevre et al. 2004), two from the spectroscopic follow-up of the K20 survey (Mignoli et al. 2005), 31 from the optical follow-up of the X-ray sources in the E-CDF-S (Silverman et al. in preparation) and one from Ravikumar et al. (2007). We report in Col. 12 of Table 3 these spectroscopic redshifts and in Col. 13 a quality flag for these measures. Since each spectroscopic survey has its own redshift quality flag system, we try to homogenize and simplify these different definitions using the following scheme: '2' secure redshift obtained using multiple spectral features, '1' tentative redshift (e.g. based on a single emission line). For radio sources with no spectroscopic information available, we collected photometric estimates of their redshifts. Due to the deep and wide photometry available in this region of the sky, reliable photometric redshifts have been produced. Almost the entire area of the VLA observations is covered by the COMBO-17 survey which provides extremely accurate photometric redshifts using photometry in 17 pass-bands from 350 to 930 nm (Wolf et al. 2004). We use this dataset with two limitations. We consider only COMBO-17 sources with $R < 24$ (Vega): at these magnitudes the errors on the photometric redshift estimates are expected to be less than $|z_{\text{phot}} - z_{\text{spec}}| / (1 + z_{\text{spec}}) \approx 0.06$. The COMBO-17 data for galaxies fainter

than $R=24$ (Vega) are too shallow. Further, we limit the use of COMBO-17 photometric redshifts to $z < 1.2$ because at higher redshifts the COMBO-17 estimates become increasingly inaccurate due to the lack of NIR coverage (see Sec. 4.6 of Wolf et al. 2004). We have waived this last constraint for objects best fitted with a QSO templates ($MC_{class} = 'QSO'$ in Wolf et al. 2004) for which the photometric redshifts are accurate at least to $z \approx 4$ (see Fig. 18 of Wolf et al. 2004). We compare our catalogue with Zheng et al. (2004) that has derived photometric redshifts for a large fraction of the X-ray sources in the CDF-S area and the GOODS-MUSIC catalogue (Grazian et al. 2006) in which are published photometric redshifts obtained using the excellent optical and NIR data in the GOODS region. In total we are able to assign photometric redshifts to 78 radio sources without spectroscopic measures: 66 from COMBO-17, nine from GOODS-MUSIC and three from Zheng et al. (2004). In order to check the accuracy of these photometric redshifts, we select only sources with a secure spectroscopic redshift (Col. 13 of Table 3 equal to 2) leading to a sample of 80 objects. In Fig. 11 (left panel) we plot the difference between the photometric and spectroscopic redshift. The photometric redshifts are extremely precise with a $|z_{\text{phot}} - z_{\text{spec}}|/(1 + z_{\text{spec}}) < 0.1$ for almost all the objects. Only three sources have larger errors: RID 221, 230, 259. The spectra of RID 221 does not leave any doubt on the correctness of the spectroscopic redshift (clear Ca H&K lines) and its photometry does not seem to be affected by near-by sources. Similarly, a further inspection of the optical spectra of RID 230 and RID 259 confirms the spectroscopic redshift $z = 1.029$ (broad MgII and CIII] emission lines) and $z = 0.860$ ([OII] and [OII] emission lines) respectively. Nevertheless, for two of these sources the disagreement between photometric and spectroscopic redshift is small (~ 0.1). Clipping these three “outliers” out, we obtain an rms = 0.013 for $|z_{\text{phot}} - z_{\text{spec}}|/(1 + z_{\text{spec}})$.

The redshift distribution of the radio sample is plotted in Fig. 11 (right panel): spectroscopic redshifts are shown as a filled histogram, the total histogram instead includes also photometric redshifts. In an inset of the same figure we show a zoom of the region $0.6 < z < 1.7$ using a finer binning in the histogram ($\Delta z = 0.02$). We note that radio sources are good tracers of large scale structures already detected at other wavebands in this region of the sky (NIR, Cimatti et al. 2002; optical, Le Fevre et al. 2004, Vanzella et al. 2005; X-ray Gilli et al. 2003, Szokoly et al. 2004). The more prominent spikes in our redshifts distribution are at $z = 0.735 \pm 0.004$ (ten objects, four of these are also X-ray sources from Giacconi et al. 2002) and $z = 1.614 \pm 0.011$ (six objects, two of these are also X-ray sources from Giacconi et al. 2002). Both these structure were traced in the X-rays (Gilli et al. 2003), respectively with 19 and 5 X-ray sources. Of the two prominent large scale structures discovered in the X-ray survey, at $z = 0.67$ and $z = 0.73$, the radio sources are tracing only the second. As noted by Gilli et al. (2003) while the structure at $z = 0.73$ is dominated by a standard galaxy cluster with a significant concentration around a central CD galaxy, the one at $z = 0.67$ appears to be a rather loose structure uniformly distributed in the field.

7. Host galaxy properties

In this section we investigate the properties of the host galaxy as a function of the 1.4 GHz flux density of the radio source. We want in particular, to study the behavior of three observables as a function of the radio flux density: a) redshift, b) morphology and c) rest-frame colors of the host galaxies. We are motivated by the known upturn in the normalized source count at 1.4 GHz below 3 mJy compared to the extrapolation from brighter flux densities (e.g. Fig. 7 in Paper I). This is generally modeled by the mix of two populations of sources: AGN and starburst galaxies. Several models (e.g. Seymour et al. 2004) predict that the starburst galaxies become dominant at 1.4 GHz flux densities below ~ 0.2 mJy. Further discussion on the source population properties will be presented by Padovani et al. (2008, Paper IV).

We divide our sample in three flux density bins with approximately the same number of sources: $S < 0.08$ mJy (91 objects), $0.08 < S < 0.2$ mJy (83 objects) and $S > 0.2$ mJy (92 objects).

a) *redshift*

In the three flux density intervals defined above respectively 71 ($\sim 78\%$), 56 ($\sim 67\%$) and 64 ($\sim 69\%$) objects have a redshift (spectroscopic or photometric). We show in Fig. 12 (left panel) the redshift distributions of the three sub-samples. The brighter objects (continuous line) are almost all at $z < 1.5$. Due to the small area of our VLA survey, we are missing the population of radio-loud QSOs that dominate this regime, as we know from shallower large-area radio surveys. The intermediate flux density bin (hatched histogram) shows a redshift distribution similar to the above one with a few objects at $z \approx 4$. A K-S test confirms with a probability of 46% that the two distributions are drawn from the same one.

Finally, the redshift distribution for the sources in the faintest bin (shaded histogram) has a tail at higher redshift ($\sim 16\%$ have $z > 1.5$). Previous surveys (e.g. Windhorst et al. 1995, Richards et al. 1998, Richards et al. 1999, Ciliegi et al. 2005) found that the majority of the μ Jy radio sources are at low ($z < 1$) redshifts. If we consider our faintest flux density bin, 22% of the objects are at $z > 1$, and for another 22% of sources we do not have any redshift information. The fraction of sources at $z > 1$ could grow up to 44% if all the unidentified objects are at high redshift. A K-S test gives a probability of 99% that the redshift distributions of the faintest and intermediate flux density bins are drawn from the same one.

b) *morphology*

In this section we investigate the morphological properties of the host galaxies. The area of our VLA observations is almost entirely covered by the GEMS survey (Rix et al. 2004). The

GEMS team has made publicly available⁶ (Häussler et al. 2007) a catalogue containing the Sersic index (n) parameter (Sersic 1968) obtained using GALFIT (Peng et al. 2002). We consider only objects in this catalogue with CONSTR_FLAG= 1 and SCIENCE_FLAG= 1 (see Haeussler et al. 2007). Applying these constraints, we are left with 60 ($S < 0.08$ mJy), 48 ($0.08 < S < 0.2$ mJy) and 34 ($S > 0.2$ mJy) objects respectively. We are therefore able to study the morphological properties of $\sim 66\%$, $\sim 58\%$ and $\sim 37\%$ of the objects in each flux density bin. The distributions of Sersic indexes are shown in Fig.12 (right panel). It has been empirically found that a Sersic index $n= 2.5$ (vertical line in Fig. 12) can roughly discriminate between early-type galaxies and late-type galaxies (e.g., Blanton et al. 2003; Shen et al. 2003; Hogg et al. 2004). Galaxies with $n > 2.5$ are generally early-type, while the majority of galaxies with $n < 2.5$ are late-type. We find that for the high and intermediate flux density bins (continuum and hatched histograms) the distribution of Sersic index is relatively flat with $\approx 55\%$ of the objects with $n > 2.5$. According to a Kolmogorov-Smirnov (K-S) test these two distributions are drawn from the same one. Instead, the distribution of Sersic indexes appears completely different for the faintest flux density bin (shaded histogram) with only $\approx 18\%$ of the sources with $n > 2.5$. A K-S test gives a probability as low as $\sim 0.05\%$ that the distribution for the faintest flux density bin and any of the other two are drawn from the same sample. This is suggesting that at ≈ 0.08 mJy there is a significant change in the radio population with late-type galaxies becoming dominant. We are aware of the fact that using only the Sersic index to divide galaxies in morphological classes could produce a mixture of different galaxy populations (e.g. Sargent et al. 2007). Therefore we visually classified our radio sources in four broad morphological categories: elliptical (E), lenticular (S0), spiral (S) and irregular (I). We show examples for these four categories in Fig. 13. We are able to classify 161 (60%) of the 266 radio sources. In Fig. 14 (left panel) we show the distribution of Sersic index values for E+S0 (hatched histogram) and S+I (shaded histogram). The distributions of Sersic indexes are clearly different for these two classes of objects (K-S probability $\approx 10^{-6}\%$): E+S0 tend to have high value of n , while S+I peak at $n < 2.5$. This plot confirms that our visual morphological classification is robust and at the same time is reassuring about the use of Sersic index to separate early and late type galaxies. We can now use this visual morphological classification to study the evolution of the host galaxy properties as a function of the $S_{1.4\text{GHz}}$ flux density. In Fig. 14 (right panel) we plot the percentages of early-type (E+S0), spiral and irregular galaxies in the three flux density bins. While a large fraction of radio sources with $S_{1.4\text{GHz}} > 0.08$ mJy are early-type, at lower flux densities late-type galaxies become five times more numerous than elliptical or lenticular galaxies.

⁶<http://www.mpia.de/GEMS/gems.htm>

c) *rest-frame colors*

We finally consider the rest-frame colors of our radio sources. We compare the list of optical/NIR counterparts presented in this work with the COMBO-17 photometric catalogue (Wolf et al. 2004). We include only COMBO-17 sources with R magnitude brighter than 24 (Vega) and we exclude sources classified as 'QSO' from the SED fitting. We further exclude sources with broad ($> 2000 \text{ km s}^{-1}$) emission lines in their optical spectra to avoid contamination by the central AGN. Removing any other potential AGN according to the criterium $L_X[0.5 - 10\text{keV}] > 10^{42} \text{ erg s}^{-1}$ does not change the result. We finally exclude sources for which the COMBO-17 redshift (that has been used to compute the rest-frame colors by Wolf et al. 2004) is not in agreement with an available spectroscopic one. We obtain rest-frame colors for 47 ($S > 0.2 \text{ mJy}$), 41 ($0.08 < S < 0.2 \text{ mJy}$) and 49 ($S < 0.08 \text{ mJy}$) objects respectively. In Fig. 15 (left panel), we plot the rest-frame U-V colors as a function of the absolute magnitude M_V for radio sources with $S > 0.2 \text{ mJy}$ (circles), $0.08 < S < 0.2 \text{ mJy}$ (triangles), $S < 0.08 \text{ mJy}$ (stars) and optically selected galaxies from COMBO-17 (grey dots). The distribution of rest-frame colors for the faintest radio flux density bin appears clearly different from the other two: while sources with $S > 0.2 \text{ mJy}$ are mainly concentrated in the top part of the plot, below 0.08 mJy the host galaxies are widely spread in the color-magnitude diagram. The dashed line in Fig.15 (left panel) is the empirical redshift-dependent color divisions that separate blue and red galaxies population. Following Bell et al. (2004), we define red-sequence/early-type galaxies as being redder than $\langle U - V \rangle = 1.15 - 0.31 \times z - 0.08(M_V - 5\log H + 20)$, where $z = 0.85$, the average redshift of our radio sample. We find that $\sim 70\%$ of the radio sources in the two brighter flux density bins are red-sequence galaxies while this percentage decreases to $\sim 40\%$ for sources with $S < 0.08 \text{ mJy}$. Again, we have an indication that early-type galaxies are the dominant population of the intermediate radio flux density bin, while late-type galaxies becomes dominant at the faintest radio flux densities. A K-S test on the distributions of the U-V colors (see right panel of Fig. 15) provides a probability as low as 0.5% for the $S < 0.08 \text{ mJy}$ colors being similar to the ones of brighter radio sources.

Recently, Bondi et al. (2007) found that between 0.15 and 0.5 mJy the median radio spectral index is significantly flatter compared to brighter or fainter sources and they interpreted this as evidence that a population of flat spectrum low luminosity compact AGNs and radio quiet QSOs is dominating the radio emission in this flux density range, while a starburst population is expected to have a steeper spectral index. At the same time, they confirm that early-type galaxies have spectral index significantly flatter than starburst ones. The Bondi et al. (2007) results are consistent with our finding that the majority of radio sources with flux densities $0.08 < S < 0.2 \text{ mJy}$ are hosted in bulge dominated early-type host galaxies while at lower radio flux densities ($S \lesssim 0.08 \text{ mJy}$) the starburst galaxies become

dominant.

8. Conclusions

We have used a likelihood ratio technique to identify the 266 radio sources from the VLA survey in the CDF-S. Using the available imaging in i , R, K_S , $3.6 \mu m$, $4.5 \mu m$, $5.8 \mu m$, $8.5 \mu m$, $24 \mu m$ and $70 \mu m$ bands we were able to find a reliable counterpart for 254 ($\sim 95\%$) radio sources. Using literature data and our own follow-up, a total of 186 ($\sim 70\%$) sources have a redshift: 108 are spectroscopic redshifts and 78 reliable photometric redshifts. The ability of obtaining a redshift (either spectroscopic or photometric) is a strong function of the magnitude of the counterparts: $\sim 88\%$ of the objects with $R_{AB} < 24$ have a redshift while this fraction decreases to $\sim 30\%$ for sources with $R_{AB} > 24$. The redshift distribution of the VLA sources peaks around $z \approx 0.9$. The radio sources are good tracers of large scale structures already detected at other wavebands in this region of the sky (NIR, optical, X-ray). In particular, the main peaks of our redshifts distribution are at $z = 0.735 \pm 0.004$ (10 objects) and $z = 1.614 \pm 0.011$ (6 objects).

We have studied the properties of the host galaxies of the radio sources dividing the sample in three flux density bins equally populated: $S > 0.2$ mJy, $0.08 < S < 0.2$ mJy and $S < 0.08$ mJy. While the properties of the host galaxies in the two brighter flux density bins look similar, we find evidences for a change in the dominant radio population at $S \approx 0.08$ mJy. The radio sources in the intermediate and bright flux density bins:

- show a Sersic indexes distribution that resembles that of early-type galaxies with a tail of disk dominated galaxies;
- according to a visual morphological classification are mainly elliptical or lenticular galaxies;
- in a rest-frame color-magnitude diagram ($U-V$ versus M_V) are preferentially (70%) located between the early-type/red-sequence galaxies;

while sources with $S < 0.08$ mJy:

- have a Sersic indexes distribution that peaks at low values of n , indicating a low value for the bulge to disk ratio, with only $\approx 18\%$ of the sources with $n > 2.5$;
- is five times more likely to be hosted in a late-type galaxy instead of an elliptical or lenticular one;

- are widely spread in the color-magnitude diagram, with $\approx 60\%$ of them not being an early-type/red-sequence galaxy.

Summarizing, we suggest that the flux density bin $S \gtrsim 0.08$ mJy is dominated by a population of early-type galaxies while at flux densities below ≈ 0.08 mJy starburst galaxies become dominant.

This work is based on observations with the National Radio Astronomy Observatory which is a facility of the National Science Foundation operated under cooperative agreement by Associated Universities, Inc. We thank the referee for constructive comments that improved the quality of the paper. We thank P. Ciliegi for enlightening discussions on the likelihood ratio technique. John Kelly assisted with the early data reduction. We acknowledge the ESO/GOODS project for the ISAAC and FORS2 data obtained using the Very Large Telescope at the ESO Paranal Observatory under Program ID(s): LP168.A-0485, 170.A-0788, 074.A-0709, and 275.A-5060. We acknowledge the GOODS team, the GOODS-MUSIC team, the COMBO-17 team, the GEMS team and the FIDEL team for making images and catalogs publicly available. PT acknowledges financial contribution from contract ASI-INAF I/023/05/0.

REFERENCES

- Afonso, J., Georgakakis, A., Almeida, C., et al., 2005, *ApJ*, 624, 135
- Afonso, J., Mobasher, B., Koekemoer, A., et al., 2006, *AJ*, 131, 1216
- Bondi, M., Ciliegi, P., Venturi, T., et al., 2007, *A&A*, 463, 519
- Brusa, M., Comastri, A., Daddi, E., et al., 2005, *A&A*, 432, 69
- Brusa, M., Zamorani, G., Comastri, A., et al., 2007, *ApJS*, 172, 353
- Ciliegi, P., et al., 1999, *MNRAS*, 302, 222
- Ciliegi, P., Zamorani, G., Hasinger, G., et al., 2003, *A&A*, 398, 901
- Ciliegi, P., Zamorani, G., Bondi, M., et al., 2005, *A&A*, 441, 879
- Cimatti, A., Mignoli, M., Daddi, E., et al., 2002, *A&A*, 392, 395
- Condon, J.J. & Mitchell, K.J., 1984, *AJ*, 89, 610

- de Ruiter, H.R., Willis A.G., & Arp, H.C., 1977, *A&A*, 28, 211
- Dickinson, M., et al., in the proceedings of the ESO/USM Workshop "The Mass of Galaxies at Low and High Redshift" (Venice, Italy, October 2001), eds. R. Bender and A. Renzini, Springer-Verlag, 2003, p. 324
- Giavalisco, M., Ferguson, H.C., Koekemoer, A.M., et al., 2004, *ApJ*, 600, L93
- Giacconi, R., Zirm, A., Wang, J.X., et al., 2002, *ApJS*, 139, 369
- Gilli, R., Cimatti, A., Daddi, E., et al., 2003, *ApJ*, 592, 721
- Grazian, A., Fontana, A., De Santis, C., et al., 2006, *A&A*, 449, 951
- Gruppioni, C., Mignoli, M., Zamorani, G., 1999, *MNRAS*, 304, 199
- Häussler, B., McIntosh, D.H., Barden, M., et al., [astro-ph/07042601]
- Kellermann, K.I., et al., 2008, submitted to *AJ* (Paper I)
- Le Fevre, O., Vettolani, G., Paltani, S., et al., 2004, *A&A*, 428, 1043
- Lehmer, B.D., Brandt, W.N., Alexander, D.M., et al., 2005, *ApJS*, 161, 21
- Mignoli, M., Cimatti, A., Zamorani, G., et al., 2005, *A&A*, 437, 883
- Olsen, L.F., Miralles, J.M., da Costa, L., et al., 2006, *A&A*, 456, 881
- Peng, Y.P., Ho, L.C., Impey, C.D., & Rix, H.-W., 2002, *AJ*, 124, 266
- Popesso, P., Dickinson, M., Nonino, M., et al. 2008, submitted to *A&A* [astro-ph/0802.2930]
- Prandoni, I., Gregorini, L., Parma, P., et al., 2001, *A&A*, 369, 787
- Prestage, R.M., & Peacock, J.A., 1983, *MNRAS*, 204, 355
- Ravikumar, C.D., et al., 2007, *A&A*, 465, 1099
- Richards, E.A., Kellermann, K.I., Fomalont, E.B., et al., 1998, *AJ*, 116, 1039
- Richards, E.A., Fomalont, E.B., Kellermann, K.I., et al., 1999, *ApJL*, 526, 73
- Richards, E.A., et al., 2000, *ApJ*, 533, 611
- Richter, G.A., 1975, *Astron. Nachrichten*, 296, 65
- Rix, H.-W., Barden, M., Beckwith, S.V.W., et al., 2004, *ApJS*, 152, 163

- Sargent, M.T., Carollo, C.M., Lilly, S.J., et al. 2007, ApJS in press, [astro-ph/0609042]
- Sersic, J.L. 1968, Atlas de Galaxias Australes (Cordoba: Obs. Astron.)
- Seymour, N., McHardy, I.M., & Gunn, K.F., 2004, MNRAS, 352, 131
- Sutherland, W., & Saunders, W., 1992, MNRAS, 259, 413
- Szokoly, G.P., Bergeron, J., Hasinger, G., et al., 2004, ApJS, 155, 271
- Thuan, T.X., & Condon, J.J., 1987, ApJ, 322, L9
- Vanzella, E., Cristiani, S., Dickinson, M., et al., 2005, A&A, 434, 53
- Vanzella, E., Cristiani, S., Dickinson, M., et al., 2006, A&A, 454, 423
- Vanzella, E., Cristiani, S., Dickinson, M., et al., 2008, A&A, 478, 83
- Windhorst, R.A., Kron, R.G., & Koo, D.C., 1984, A&ASS, 58, 39
- Windhorst, R.A., Miley, G.K., Owen, F.N., 1985, ApJ, 289, 494
- Windhorst, R.A., Fomalont, E.B., Kellermann, K.I., et al., 1995, Nature, 375, 471
- Wolf, C., Meisenheimer, K., Kleinheinrich, M., et al., 2004, A&A, 421, 913
- Wolstencroft, R.D., Savage, A., Clowes, R.G., et al., 1986, MNRAS, 223,279
- Zheng, W., Mikles, V.J., Mainieri, V., et al., 2004, ApJS, 155, 73

Table 1: Positional offsets between the radio and the optical/nearIR catalogs.

	Optical		NIR	
	ACS-i	WFI-R	ISAAC-K	SOFI-K
$\langle \Delta RA \rangle$:	0.15''	0.20''	0.15''	0.13''
$\langle \Delta Dec \rangle$:	0.12''	0.09''	-0.23''	0.12''

Table 2: Output of the likelihood ratio technique for the radio sources identification.

	Optical		NIR		Total
	ACS-i	WFI-R	ISAAC-K	SOFI-K	
radio sources ^a :	79	266	61	266	266
LR>LR _{th} counterparts ^b :	67	230	56	190	254
LR<LR _{th} counterparts ^c :	4	24	1	12	9
frac. identified ^d :	85%	86%	92%	71%	95%
possible spurious ^e :	< 1	3	< 1	6	8
unidentified ^f :	12	36	5	76	12
empty fields ^g :	8	12	4	64	3

^a Number of radio sources inside the area imaged in the different bands

^b Number of radio sources with a counterpart with LR above the threshold LR>LR_{th} and therefore considered reliable.

^c Number of radio sources only with a counterpart with LR below the threshold LR<LR_{th} and therefore considered unreliable.

^d Percentage of identified sources (considering only counterparts with LR>LR_{th}).

^e Maximum number of spurious sources expected between the counterparts with LR>LR_{th}.

^f Number of radio sources without any counterparts or with counterparts with LR<LR_{th}.

^g Number of radio sources without any possible counterpart.

Table 3. Optical, near infrared primary counterparts of the 20 cm sources in the E-CDF-S

(1)	RADIO		OPTICAL		(6)	(7)	(8)	(9)	(10)	(11)	(12)	(13)	(14)
RID	(2)	(3)	(4)	(5)	(6)	(7)	(8)	(9)	(10)	(11)	(12)	(13)	(14)
	RA	Dec	RA	Dec	dist	LR	Rel	catalogue	R	K	z	Qual-z	z_{phot}
	(J2000)		(J2000)		(")				(AB)	(AB)			
1	3:31:11.70	-27:31:44.3	3:31:11.64	-27:31:43.5	0.90	101.25	1.00	WFI-R	16.79±0.01	>21.4			
2	3:31:13.96	-27:39:10.3	3:31:13.98	-27:39:10.4	0.40	29.79	0.99	WFI-R	23.13±0.04	>21.4			
3	3:31:14.20	-27:48:44.3	3:31:14.12	-27:48:44.2	1.00	0.85	0.81	WFI-R	25.12±0.19	>21.4			
4	3:31:14.42	-27:39:07.1	3:31:14.53	-27:39:06.6	1.60	35.25	0.99	WFI-R	18.04±0.01	>21.4			
5	3:31:14.50	-27:55:46.3	3:31:14.46	-27:55:46.6	0.60	19.06	0.99	WFI-R	23.40±0.03	>21.4			
6	3:31:14.87	-27:55:43.4	3:31:14.91	-27:55:41.5	2.00	1.60	0.89	WFI-R	23.28±0.03	>21.4			
7	3:31:15.06	-27:55:18.4	3:31:15.04	-27:55:18.6	0.30	67.91	1.00	WFI-R	20.84±0.01	>21.4			0.49±0.03 ¹
8	3:31:16.00	-27:44:43.2	3:31:15.98	-27:44:43.2	0.10	21.47	0.98	WFI-R	23.98±0.04	>21.4			0.86±0.04 ¹
9	3:31:17.36	-28:01:47.8	3:31:17.34	-28:01:47.0	0.70	63.25	1.00	WFI-R	20.98±0.01	>21.4			0.67±0.02 ¹
10	3:31:18.74	-27:49:02.4	3:31:18.62	-27:49:03.1	1.70	0.30	0.60	WFI-R	26.00±0.10	>21.4			
11	3:31:19.92	-27:35:50.2	3:31:19.88	-27:35:49.3	1.00	21.29	0.99	WFI-R	21.62±0.01	>21.4			0.90±0.01 ¹
12	3:31:20.12	-27:39:01.3	3:31:20.15	-27:39:01.2	0.50	128.81	1.00	WFI-R	20.30±0.01	>21.4			0.55±0.02 ¹
13	3:31:23.32	-27:49:06.4	3:31:23.30	-27:49:05.8	0.50	31.86	0.99	WFI-R	22.70±0.02	>21.4			1.00±0.04 ¹
14	3:31:24.94	-27:52:08.5	3:31:24.88	-27:52:07.5	1.10	33.52	0.99	WFI-R	20.11±0.01	>21.4			
15	3:31:25.31	-27:59:59.4	3:31:25.29	-27:59:58.7	0.60	19.22	0.99	WFI-R	22.96±0.02	>21.4			0.79±0.08 ¹
16	3:31:27.07	-27:59:58.6	3:31:27.07	-27:59:57.4	1.10	3.46	0.95	WFI-R	23.90±0.09	>21.4			
17	3:31:27.07	-27:44:10.4	3:31:27.06	-27:44:09.5	0.80	14.83	0.99	WFI-R	23.10±0.02	>21.4			0.55±0.00 ¹
18	3:31:27.23	-27:42:47.6	3:31:27.20	-27:42:46.5	1.10	2.68	0.93	WFI-R	24.23±0.05	>21.4			
19	3:31:27.58	-27:44:39.5	3:31:27.55	-27:44:39.1	0.60	0.30	0.60	GEMS-z	>25.5	>21.4			
20	3:31:28.60	-27:49:35.6	3:31:28.60	-27:49:34.9	0.70	25.43	0.99	WFI-R	22.77±0.01	>21.4	0.846 ^b	2	0.83±0.03 ¹
21	3:31:29.80	-27:32:18.7	3:31:29.78	-27:32:18.4	0.30	42.28	1.00	WFI-R	22.75±0.02	>21.4			
22	3:31:29.88	-27:57:22.7	3:31:29.84	-27:57:22.5	0.50	0.37	0.65	WFI-R	26.11±0.29	>21.4			
23	3:31:30.05	-27:38:14.2	3:31:29.98	-27:38:14.6	0.90	0.30	0.60	WFI-R	26.00±0.10*	>21.4			
24	3:31:30.15	-27:56:01.9	3:31:30.06	-27:56:02.4	1.20	29.96	0.99	WFI-R	19.91±0.01	>21.4			0.69±0.01 ¹
25	3:31:30.79	-27:57:34.7	3:31:30.73	-27:57:34.9	0.70	11.12	0.98	WFI-R	23.86±0.04	>21.4			1.06±0.17 ¹
26	3:31:32.87	-28:01:16.6	3:31:32.82	-28:01:15.9	0.90	142.48	1.00	WFI-R	17.71±0.01	>21.4			0.15±0.01 ¹
27	3:31:34.26	-27:38:28.7	3:31:34.21	-27:38:28.5	0.50	27.83	0.99	WFI-R	22.93±0.03	>21.4			1.08±0.06 ¹
28	3:31:37.77	-27:51:41.8	3:31:37.73	-27:51:40.9	0.90	30.62	0.99	WFI-R	21.24±0.01	>21.4			0.36±0.04 ¹
29	3:31:38.47	-27:59:41.9	3:31:38.67	-27:59:41.1	2.80	0.01	0.01	WFI-R	25.20±0.12	>21.4			
30	3:31:38.56	-27:38:08.8	3:31:38.41	-27:38:10.4	2.60	0.01	0.01	WFI-R	25.00±0.10	>21.4			
31	3:31:39.52	-27:41:19.1	3:31:39.50	-27:41:19.6	0.60	19.20	0.99	WFI-R	23.04±0.02	>21.4			

Table 3—Continued

(1) RID	RADIO		OPTICAL		(6) dist (")	(7) LR	(8) Rel	(9) catalogue	(10) R (AB)	(11) K (AB)	(12) z	(13) Qual-z	(14) z_{phot}
	(2) RA (J2000)	(3) Dec	(4) RA (J2000)	(5) Dec									
32	3:31:40.10	-27:36:48.1	3:31:40.05	-27:36:47.7	0.60	30.25	0.99	WFI-R	21.78±0.01	>21.4			0.69±0.03 ¹
33	3:31:43.24	-27:54:05.1	3:31:43.22	-27:54:05.5	0.50	2.40	0.92	WFI-R	25.15±0.12	>21.4			
34	3:31:43.37	-27:51:01.9	3:31:43.33	-27:51:02.0	0.50	215.34	1.00	WFI-R	19.06±0.01	>21.4			0.26±0.03 ¹
35	3:31:43.42	-27:42:48.9	3:31:43.43	-27:42:48.6	0.20	64.55	1.00	WFI-R	21.34±0.01	>21.4	0.466 ^d	2	0.47±0.01 ¹
36	3:31:43.56	-27:55:28.0	3:31:43.59	-27:55:28.1	0.50	294.56	1.00	WFI-R	17.80±0.01	17.78±0.07			0.11±0.01 ¹
37	3:31:44.05	-27:38:35.0	3:31:43.96	-27:38:35.2	1.10	5.28	0.96	WFI-R	23.41±0.03	>21.4			0.06±0.04 ¹
38	3:31:44.48	-27:42:11.0	3:31:44.45	-27:42:12.1	1.20	5.90	0.85	WFI-R	23.49±0.03	20.93±0.36			0.83±0.05 ¹
39	3:31:46.00	-27:51:30.0	3:31:45.97	-27:51:30.1	0.40	39.28	0.99	WFI-R	22.25±0.01	19.50±0.05	0.681 ^a	0	0.65±0.04 ¹
40	3:31:46.09	-28:00:26.0	3:31:46.09	-28:00:26.4	0.40	9.08	0.97	WFI-R	24.45±0.07	>21.4			
41	3:31:46.56	-27:57:34.0	3:31:46.57	-27:57:34.7	0.80	83.38	1.00	WFI-R	20.07±0.01	17.96±0.03			0.36±0.02 ¹
42	3:31:47.39	-27:45:42.0	3:31:47.38	-27:45:41.7	0.20	2.54	0.93	WFI-R	25.31±0.17	21.18±0.20			
43	3:31:47.66	-27:50:14.0	3:31:47.66	-27:50:13.7	0.30	64.36	1.00	WFI-R	21.25±0.01	18.98±0.03			0.54±0.02 ¹
44	3:31:47.86	-27:54:52.0	3:31:47.77	-27:54:52.0	1.20	1.82	0.90	WFI-R	24.49±0.08	20.82±0.13			
45	3:31:49.70	-27:43:25.6	3:31:49.69	-27:43:26.3	0.80	60.74	1.00	WFI-R	20.80±0.01	18.49±0.02	0.618 ^d	2	0.60±0.02 ¹
46	3:31:49.86	-27:48:38.0	3:31:49.87	-27:48:38.6	0.70	2.33	0.92	GEMS-z	>25.5	19.13±0.02			
47	3:31:50.03	-27:58:06.1	3:31:50.01	-27:58:06.2	0.30	8.77	0.97	WFI-R	24.43±0.06	>21.4			
48	3:31:50.08	-27:39:47.2	3:31:50.15	-27:39:48.1	1.40	1.00	0.83	WFI-R	23.71±0.05	20.11±0.09			1.13±0.12 ¹
49	3:31:50.33	-27:58:18.1	3:31:50.30	-27:58:18.9	1.00	0.44	0.69	WFI-R	25.61±0.20	>21.4			
50	3:31:50.35	-27:41:19.1	3:31:50.33	-27:41:20.2	1.10	25.47	0.99	SOFI-K	23.94±0.03	20.64±0.07	1.791 ^d	1	0.70±0.09 ^{1*}
51	3:31:50.78	-27:47:03.1	3:31:50.78	-27:47:03.5	0.50	21.99	0.99	WFI-R	23.60±0.03	21.07±0.13			
52	3:31:51.09	-27:44:36.4	3:31:51.10	-27:44:37.3	1.00	7.65	0.97	WFI-R	23.66±0.04	20.37±0.08			0.85±0.19 ¹
53	3:31:51.32	-27:50:56.0	3:31:51.28	-27:50:56.0	0.50	79.54	1.00	SOFI-K	24.26±0.07	20.64±0.20			
54	3:31:51.94	-27:53:26.1	3:31:51.94	-27:53:27.0	1.00	1.41	0.88	WFI-R	24.74±0.10	22.24±0.42	2.940 ^a	2	
55	3:31:52.08	-27:43:21.1	3:31:52.00	-27:43:21.3	1.00	10.66	0.97	WFI-R	22.94±0.03	22.25±0.22	1.501 ^d	2	
56	3:31:52.10	-27:39:25.1	3:31:52.16	-27:39:26.6	1.60	1.10	0.85	SOFI-K	24.55±0.06	21.81±0.23			
57	3:31:52.82	-27:44:29.1	3:31:52.77	-27:44:30.4	1.50	0.14	0.40	WFI-R	25.19±0.14	>21.4			
58	3:31:53.41	-28:02:21.0	3:31:53.42	-28:02:21.1	0.30	15.33	0.99	WFI-R	23.96±0.09	>21.4			0.96±0.11 ¹
59	3:31:54.08	-27:50:03.9	3:31:54.05	-27:50:05.6	1.80	3.08	0.94	WFI-R	21.85±0.01	19.35±0.05			0.71±0.04 ¹
60	3:31:54.90	-27:53:40.5	3:31:54.75	-27:53:41.3	2.00	0.09	0.32	WFI-R	24.46±0.10	21.67±0.34			
61	3:31:55.00	-27:44:10.1	3:31:54.98	-27:44:10.5	0.50	15.21	0.98	WFI-R	23.93±0.05	20.02±0.06	0.758 ^e	1	
62	3:31:56.31	-27:40:00.5	3:31:56.29	-27:40:00.6	0.20	41.88	1.00	SOFI-K	>25.5	21.78±0.21			

Table 3—Continued

(1) RID	RADIO		OPTICAL		(6) dist (")	(7) LR	(8) Rel	(9) catalogue	(10) R (AB)	(11) K (AB)	(12) z	(13) Qual-z	(14) z_{phot}
	(2) RA (J2000)	(3) Dec (J2000)	(4) RA (J2000)	(5) Dec (J2000)									
63	3:31:56.45	-27:52:36.1	3:31:56.43	-27:52:36.6	0.60	12.51	0.98	WFI-R	23.86±0.04	20.06±0.08			0.77±0.08 ¹
64	3:31:56.77	-27:52:25.2	3:31:56.71	-27:52:25.5	0.90	32.09	0.99	SOFI-K	>25.5	21.13±0.11			
65	3:31:56.97	-27:59:39.2	3:31:56.87	-27:59:39.2	1.20	0.41	0.67	WFI-R	25.22±0.12	>21.4			
66	3:31:57.80	-27:42:07.4	3:31:57.79	-27:42:08.7	1.40	4.44	0.96	WFI-R	22.32±0.01	19.34±0.04	0.665 ^d	2	0.65±0.03 ¹
67	3:31:58.21	-27:38:15.2	3:31:58.20	-27:38:16.5	1.40	2.37	0.86	WFI-R	23.91±0.04	>21.4			
68	3:31:58.29	-27:50:41.4	3:31:58.27	-27:50:41.9	0.60	1.18	0.83	WFI-R	25.16±0.08	21.40±0.25			1.99±0.23 ³
69	3:31:58.93	-27:43:03.2	3:31:58.91	-27:43:04.1	1.10	33.20	0.99	ACS-i	23.19±0.03	20.15±0.08			0.81±0.08 ¹
70	3:31:59.82	-27:45:40.3	3:31:59.85	-27:45:40.3	0.00	10.00	0.90	SPITZER	>27.5	>24.7			
71	3:32:00.84	-27:35:56.4	3:32:00.84	-27:35:56.8	0.50	32.57	0.96	WFI-R	22.90±0.02	>21.4			0.95±0.04 ¹
72	3:32:01.29	-27:53:36.4	3:32:01.29	-27:53:36.5	0.10	12.97	0.98	SOFI-K	>25.5	22.35±0.29			
73	3:32:01.47	-27:46:47.9	3:32:01.42	-27:46:47.0	1.10	35.88	0.99	SOFI-K	>25.5	19.95±0.09			
74	3:32:02.86	-27:56:12.3	3:32:02.81	-27:56:12.8	0.80	31.56	0.99	SOFI-K	>25.5	21.36±0.19			
75	3:32:03.34	-27:53:14.3	3:32:03.22	-27:53:12.8	2.20	0.22	0.52	SOFI-K	24.95±0.12	21.91±0.33			
76	3:32:03.65	-27:46:04.0	3:32:03.65	-27:46:03.7	0.30	324.86	1.00	ACS-i	20.99±0.01	18.51±0.02	0.574 ^a	2	0.59±0.00 ¹
77	3:32:03.85	-27:58:04.4	3:32:03.87	-27:58:05.4	1.20	0.66	0.77	WFI-R	24.98±0.14	>21.4			
78	3:32:04.67	-28:00:57.3	3:32:04.69	-28:00:57.7	0.50	6.56	0.90	GEMS-z	24.34±0.06	>21.4			
79	3:32:04.80	-27:46:48.3	3:32:04.84	-27:46:47.6	0.90	2.06	0.87	ACS-i	26.10±0.10	21.26±0.19			
80	3:32:06.12	-27:32:36.1	3:32:06.09	-27:32:35.5	0.60	32.17	0.99	WFI-R	22.44±0.02	>21.4			
81	3:32:06.34	-27:56:26.3	3:32:06.32	-27:56:26.4	0.30	75.80	1.00	SOFI-K	>25.5	20.96±0.14			0.50±0.01 ¹
82	3:32:06.45	-27:47:29.3	3:32:06.44	-27:47:28.8	0.40	182.38	1.00	ACS-i	22.71±0.01	19.56±0.03	1.021 ^b	2	1.00±0.04 ¹
83	3:32:07.27	-27:51:21.2	3:32:07.32	-27:51:20.4	1.10	4.31	0.95	WFI-R	23.98±0.03	20.81±0.07	0.034 ^d	1	0.80±0.18 ¹
84	3:32:08.56	-27:46:48.4	3:32:08.53	-27:46:48.3	0.20	1422.87	1.00	ACS-i	19.45±0.01	17.06±0.01	0.310 ^a	2	0.33±0.00 ¹
85	3:32:08.70	-27:47:34.4	3:32:08.66	-27:47:34.4	0.40	887.95	1.00	ACS-i	18.98±0.01	17.59±0.01	0.544 ^a	2	0.58±0.02 ¹
86	3:32:09.70	-27:42:48.2	3:32:09.71	-27:42:48.1	0.20	397.46	1.00	ACS-i	21.96±0.01	19.71±0.04	0.733 ^a	2	0.76±0.01 ¹
87	3:32:09.90	-27:50:15.7	3:32:09.85	-27:50:15.5	1.00	10.00	0.90	SPITZER	>27.5	>24.7			
88	3:32:10.16	-27:59:38.4	3:32:10.14	-27:59:38.3	0.10	77.83	1.00	WFI-R	21.27±0.01	>21.4			0.65±0.02 ¹
89	3:32:10.73	-27:48:07.4	3:32:10.72	-27:48:07.1	0.20	125.28	1.00	ACS-i	23.04±0.03	19.97±0.01	0.653 ^b	2	0.65±0.08 ²
90	3:32:10.81	-27:59:26.4	3:32:10.82	-27:59:26.8	0.50	104.84	1.00	WFI-R	20.85±0.01	>21.4	0.651 ^g	1	0.66±0.01 ¹
91	3:32:10.82	-27:46:28.2	3:32:10.79	-27:46:27.8	0.30	34.13	0.99	ACS-i	24.59±0.08	20.01±0.02	1.610 ^f	2	1.61±0.08 ²
92	3:32:10.91	-27:44:15.2	3:32:10.91	-27:44:14.9	0.20	150.27	1.00	ACS-i	22.50±0.01	20.75±0.01	1.615 ^a	2	1.62±0.08 ²
93	3:32:11.00	-27:40:53.3	3:32:10.99	-27:40:53.7	0.50	31.37	0.99	ACS-i	24.60±0.10	21.35±0.18	0.181 ^a	2	

Table 3—Continued

(1) RID	RADIO		OPTICAL			(6) dist (")	(7) LR	(8) Rel	(9) catalogue	(10) R (AB)	(11) K (AB)	(12) z	(13) Qual-z	(14) z_{phot}
	(2) RA (J2000)	(3) Dec (J2000)	(4) RA (J2000)	(5) Dec (J2000)										
94	3:32:11.50	-27:48:16.1	3:32:11.49	-27:48:15.6	0.30	627.69	1.00	ACS-i	20.42±0.01	18.22±0.01	0.547 ^b	2	0.55±0.08 ²	
95	3:32:11.53	-27:47:13.5	3:32:11.51	-27:47:13.1	0.30	282.46	1.00	ACS-i	22.02±0.01	19.44±0.01	0.576 ^f	2	0.58±0.08 ²	
96	3:32:11.67	-27:37:26.3	3:32:11.64	-27:37:26.0	0.30	406.92	1.00	WFI-R	18.88±0.01	>21.4			1.57±0.09 ¹	
97	3:32:13.09	-27:43:50.7												
98	3:32:13.19	-27:57:44.4	3:32:13.15	-27:57:44.5	0.50	8.26	0.86	WFI-R	24.36±0.04	>21.4			1.05±0.17 ¹	
99	3:32:13.26	-27:42:40.9	3:32:13.25	-27:42:40.9	0.10	667.01	1.00	ACS-i	20.40±0.01	18.54±0.01	0.605 ^a	2	0.61±0.08 ²	
100	3:32:13.31	-27:39:34.1	3:32:13.36	-27:39:34.8	1.00	10.00	0.90	SPITZER	>25.5	>21.4				
101	3:32:13.52	-27:49:52.5	3:32:13.48	-27:49:52.8	0.60	63.55	0.82	ACS-i	22.78±0.02	19.80±0.01			0.05±0.08 ²	
102	3:32:14.14	-27:49:10.4	3:32:14.13	-27:49:10.1	0.20	22.03	0.99	ACS-i	24.44±0.06	22.47±0.05	2.076 ^b	2	2.18±0.08 ²	
103	3:32:14.80	-27:56:40.3	3:32:14.82	-27:56:40.5	0.40	119.04	1.00	WFI-R	20.90±0.01	17.81±0.02	0.733 ^d	2	0.73±0.03 ¹	
104	3:32:15.37	-27:37:06.4	3:32:15.41	-27:37:06.3	0.70	3.61	0.95	WFI-R	24.63±0.11	>21.4				
105	3:32:15.39	-27:50:37.5	3:32:15.30	-27:50:37.5	1.00	10.00	0.90	SPITZER	>27.5	>24.7				
106	3:32:15.96	-27:34:38.5	3:32:15.96	-27:34:38.2	0.30	39.53	0.99	WFI-R	23.01±0.03	>21.4			0.76±0.01 ¹	
107	3:32:17.06	-27:58:46.4	3:32:17.10	-27:58:47.4	1.20	0.90	0.82	WFI-R	24.59±0.10	>21.4				
108	3:32:17.09	-27:43:03.4	3:32:17.14	-27:43:03.3	0.90	150.78	1.00	ACS-i	21.29±0.01	19.48±0.01	0.569 ^a	2	0.57±0.08 ²	
109	3:32:17.13	-27:59:17.3	3:32:17.06	-27:59:16.6	1.10	76.23	1.00	WFI-R	18.10±0.01	>21.4			0.14±0.00 ¹	
110	3:32:17.22	-27:52:21.3	3:32:17.17	-27:52:20.8	0.60	80.24	0.99	ACS-i	23.57±0.03	20.10±0.01	1.097 ^a	2	1.10±0.08 ²	
111	3:32:17.89	-27:50:59.4	3:32:17.87	-27:50:59.3	0.10	510.88	1.00	ACS-i	18.92±0.01	16.97±0.01	0.124 ^e	2	0.12±0.08 ²	
112	3:32:18.05	-27:47:19.3	3:32:18.02	-27:47:18.5	0.70	379.13	1.00	ACS-i	21.08±0.01	17.77±0.01	0.734 ^a	2	0.73±0.08 ²	
113	3:32:19.17	-27:54:07.7	3:32:19.29	-27:54:06.1	2.20	0.39	0.01	ACS-i	22.17±0.01	18.58±0.01	0.964 ^a	2	1.12±0.08 ²	
114	3:32:19.42	-27:52:17.8	3:32:19.52	-27:52:17.7	1.40	4.76	0.96	ACS-i	23.70±0.04	20.10±0.01			1.00±0.08 ²	
115	3:32:19.79	-27:41:22.3	3:32:19.81	-27:41:22.7	0.70	680.55	1.00	ACS-i	19.41±0.01	17.94±0.01	0.229 ^a	2	0.23±0.08 ²	
116	3:32:19.91	-27:57:21.3	3:32:19.90	-27:57:20.4	0.80	16.66	0.99	WFI-R	22.72±0.02	19.70±0.10			0.70±0.03 ¹	
117	3:32:20.24	-27:52:22.5	3:32:20.26	-27:52:22.0	0.50	317.01	1.00	ACS-i	20.63±0.01	18.73±0.01	0.343 ^a	2	0.46±0.08 ²	
118	3:32:21.00	-27:47:06.3	3:32:20.92	-27:47:05.4	1.20	83.16	0.91	ACS-i	20.94±0.01	18.81±0.01	0.670 ^b	2	0.67±0.08 ²	
119	3:32:21.08	-27:35:30.4	3:32:21.08	-27:35:30.0	0.30	50.82	1.00	WFI-R	22.14±0.01	>21.4			0.71±0.03 ¹	
120	3:32:21.29	-27:44:35.6	3:32:21.28	-27:44:35.6	0.20	443.73	0.86	ACS-i	20.53±0.01	18.22±0.01	0.524 ^b	2	0.52±0.08 ²	
121	3:32:22.04	-27:42:44.0	3:32:22.01	-27:42:43.3	0.60	10.94	0.79	ACS-i	25.56±0.11	21.61±0.04			2.12±0.08 ²	
122	3:32:22.49	-27:48:05.4	3:32:22.50	-27:48:04.7	0.50	9.37	0.98	ISAAC-K	25.07±0.14	22.77±0.07				
123	3:32:22.52	-27:49:34.1	3:32:22.48	-27:49:35.0	1.10	39.15	0.99	ACS-i	22.78±0.02	19.57±0.01	0.731 ^b	2	0.67±0.08 ²	
124	3:32:22.58	-28:00:24.3	3:32:22.59	-28:00:23.4	0.80	139.35	1.00	WFI-R	17.47±0.01	>21.4			0.13±0.01 ¹	

Table 3—Continued

(1) RID	RADIO		OPTICAL		(6) dist (")	(7) LR	(8) Rel	(9) catalogue	(10) R (AB)	(11) K (AB)	(12) z	(13) Qual-z	(14) z_{phot}
	(2) RA (J2000)	(3) Dec	(4) RA (J2000)	(5) Dec									
156	3:32:35.75	-27:49:16.4	3:32:35.71	-27:49:16.0	0.40	13.89	0.99	ACS-i	24.96±0.11	21.85±0.02	2.579 ^b	1	2.58±0.08 ²
157	3:32:36.20	-27:49:32.5	3:32:36.17	-27:49:31.8	0.50	318.14	1.00	ACS-i	21.19±0.01	18.92±0.01	0.547 ^a	2	0.55±0.08 ²
158	3:32:36.51	-27:34:53.8	3:32:36.53	-27:34:53.5	0.40	11.06	0.98	WFI-R	23.99±0.05	>21.4			
159	3:32:37.24	-27:57:49.2	3:32:37.22	-27:57:48.1	1.00	104.07	1.00	WFI-R	18.43±0.01	17.20±0.03			0.13±0.01 ¹
160	3:32:37.29	-27:51:27.4	3:32:37.34	-27:51:27.4	0.90	75.51	0.81	ACS-i	21.59±0.01	19.71±0.01			0.52±0.08 ²
161	3:32:37.79	-27:50:00.4	3:32:37.74	-27:50:00.4	0.60	22.61	0.77	ACS-i	23.95±0.05	21.24±0.02	1.619 ^c	2	1.62±0.08 ²
162	3:32:37.80	-27:52:12.4	3:32:37.76	-27:52:12.3	0.30	28.48	0.98	ACS-i	24.68±0.05	20.60±0.01	1.603 ^a	2	1.60±0.08 ²
163	3:32:38.79	-27:49:56.5	3:32:38.82	-27:49:56.3	0.50	453.77	1.00	ACS-i	20.39±0.01	18.39±0.01	0.242 ^a	2	0.24±0.08 ²
164	3:32:38.80	-27:44:49.2	3:32:38.79	-27:44:48.9	0.10	111.16	1.00	ACS-i	22.92±0.01	19.98±0.01	0.736 ^d	2	0.59±0.08 ²
165	3:32:38.94	-27:57:00.4	3:32:38.94	-27:57:00.7	0.40	281.10	1.00	WFI-R	18.96±0.01	17.33±0.02	0.298 ^d	2	0.30±0.00 ¹
166	3:32:38.95	-27:59:19.4	3:32:38.88	-27:59:18.7	1.10	10.67	0.98	WFI-R	22.35±0.01	>21.4	0.652 ^e	1	
167	3:32:39.19	-27:53:57.4	3:32:39.19	-27:53:57.7	0.50	185.08	1.00	ACS-i	21.94±0.01	20.05±0.01			0.61±0.08 ²
168	3:32:39.47	-27:54:11.3	3:32:39.41	-27:54:11.8	0.90	15.64	0.99	ACS-i	23.72±0.07	19.98±0.01	1.295 ^c	2	1.29±0.08 ²
169	3:32:39.47	-27:53:01.3	3:32:39.48	-27:53:01.6	0.60	230.83	0.54	ACS-i	21.25±0.01	18.91±0.01	0.686 ^c	2	0.69±0.08 ²
170	3:32:39.68	-27:48:51.4	3:32:39.67	-27:48:50.6	0.60	13.19	0.86	ACS-i	25.18±0.09	21.61±0.03	3.064 ^a	2	3.04±0.08 ²
171	3:32:39.74	-28:03:11.9	3:32:39.70	-28:03:11.4	0.80	10.00	0.90	WFI-R	24.00±0.01	>21.4			
172	3:32:40.76	-27:55:05.3	3:32:40.76	-27:55:05.4	0.30	219.30	1.00	ACS-i	22.27±0.01	19.63±0.05	0.978 ^c	2	0.98±0.08 ²
173	3:32:40.87	-27:55:46.2	3:32:40.84	-27:55:46.7	0.70	2.55	0.93	ACS-i	25.60±0.13	21.38±0.26	0.625 ^a	1	0.62±0.08 ²
174	3:32:41.65	-28:01:28.3	3:32:41.61	-28:01:27.7	0.60	23.22	0.99	WFI-R	23.13±0.02	>21.4			0.61±0.07 ¹
175	3:32:42.00	-27:39:49.3	3:32:41.99	-27:39:49.3	0.10	309.27	1.00	WFI-R	19.01±0.01	17.28±0.01	0.152 ^b	2	0.15±0.01 ¹
176	3:32:42.57	-27:38:16.4	3:32:42.63	-27:38:16.0	0.90	0.52	0.72	GEMS-z	>25.5	>21.4			
177	3:32:43.16	-27:55:14.3	3:32:43.17	-27:55:14.7	0.60	19.16	0.98	ACS-i	23.83±0.05	21.44±0.31	0.579 ^d	1	
178A	3:32:44.20	-27:51:42.1	3:32:44.27	-27:51:41.1	1.30	78.66	0.99	ACS-i	19.99±0.01	18.09±0.01	0.279 ^a	2	0.28±0.08 ²
178B	3:32:44.20	-27:51:42.1	3:32:44.05	-27:51:43.3	2.20	0.31	0.00	ACS-i	19.34±0.01	17.12±0.01	0.279 ^a	2	0.28±0.08 ²
179	3:32:44.22	-27:57:45.2	3:32:44.23	-27:57:44.5	0.60	19.43	0.99	WFI-R	23.12±0.03	20.19±0.26			1.09±0.04 ¹
180	3:32:44.88	-27:47:28.0	3:32:44.87	-27:47:27.6	0.30	396.27	1.00	ACS-i	19.07±0.01	17.57±0.01			0.19±0.03 ¹
181	3:32:44.98	-27:54:39.3	3:32:45.02	-27:54:39.6	0.80	818.33	1.00	ACS-i	19.69±0.01	18.00±0.01	0.459 ^a	2	0.46±0.08 ²
182	3:32:45.38	-28:04:50.3	3:32:45.34	-28:04:49.8	0.60	9.06	0.97	WFI-R	24.17±0.09	>21.4			
183	3:32:45.96	-27:57:44.4	3:32:45.96	-27:57:45.4	1.10	72.92	1.00	WFI-R	17.05±0.01	16.04±0.02	0.103 ^d	2	0.12±0.03 ³
184	3:32:45.96	-27:53:16.2	3:32:45.96	-27:53:15.7	0.40	1.45	0.88	WFI-R	25.47±0.19	>24.7			2.31±0.08 ²
185	3:32:46.33	-27:53:27.3	3:32:46.33	-27:53:27.0	0.30	20.03	0.99	ACS-i	25.13±0.13	21.35±0.03			1.99±0.08 ²

Table 3—Continued

(1) RID	RADIO		OPTICAL		(6) dist (")	(7) LR	(8) Rel	(9) catalogue	(10) R (AB)	(11) K (AB)	(12) z	(13) Qual-z	(14) z_{phot}
	(2) RA (J2000)	(3) Dec	(4) RA (J2000)	(5) Dec									
186	3:32:46.83	-27:42:15.1	3:32:46.77	-27:42:11.9	3.20	10.00	0.90	WFI-R	16.26±0.01	14.98±0.01	0.103 ^a	2	0.12±0.00 ¹
187	3:32:46.86	-27:51:21.2	3:32:46.84	-27:51:21.2	0.20	38.90	0.99	ACS-i	24.20±0.04	21.93±0.06	2.292 ^d	1	1.33±0.08 ²
188	3:32:46.97	-27:39:02.3	3:32:46.95	-27:39:03.0	0.80	156.17	1.00	WFI-R	17.60±0.01	16.18±0.01	0.152 ^b	2	0.17±0.01 ¹
189	3:32:47.35	-27:42:47.5	3:32:47.29	-27:42:48.3	1.10	50.10	1.00	ACS-i	21.92±0.01	19.38±0.04	0.730 ^d	2	
190	3:32:47.88	-27:42:32.4	3:32:47.91	-27:42:32.9	0.70	32.84	0.99	WFI-R	21.65±0.01	18.92±0.04	0.979 ^a	2	0.99±0.02 ¹
191	3:32:48.30	-27:56:26.3	3:32:48.30	-27:56:26.9	0.70	140.33	1.00	WFI-R	19.20±0.01	17.35±0.01	0.346 ^d	2	0.34±0.01 ¹
192	3:32:48.59	-27:49:34.4	3:32:48.57	-27:49:34.3	0.10	25.00	0.95	ACS-i	24.64±0.11	21.07±0.02	1.120 ^c	2	1.06±0.08 ²
193	3:32:49.20	-27:40:49.8	3:32:49.22	-27:40:50.4	0.70	21.91	0.99	WFI-R	22.61±0.02	19.63±0.05	0.546 ^e	1	
194	3:32:49.35	-27:58:44.4	3:32:49.36	-27:58:45.8	1.50	0.82	0.80	WFI-R	24.23±0.08	>21.4			
195	3:32:49.45	-27:42:35.1	3:32:49.43	-27:42:35.1	0.20	23.09	0.99	WFI-R	23.86±0.05	20.55±0.21	0.981 ^e	2	
196	3:32:49.89	-27:34:46.0	3:32:49.95	-27:34:45.7	0.90	88.85	1.00	WFI-R	19.23±0.01	>21.4			0.25±0.01 ¹
197	3:32:49.96	-27:34:32.4	3:32:49.97	-27:34:32.6	0.40	268.07	1.00	WFI-R	18.40±0.01	>21.4	0.251 ^b	2	0.24±0.01 ¹
198	3:32:51.71	-27:39:35.1	3:32:51.67	-27:39:36.8	1.90	1.18	0.85	WFI-R	23.33±0.02	21.70±0.27	0.780 ^b	1	
199	3:32:51.78	-27:59:56.5	3:32:51.80	-27:59:56.2	0.40	27.86	0.99	WFI-R	22.50±0.02	>21.4			0.55±0.05 ¹
200	3:32:51.81	-27:44:36.6	3:32:51.84	-27:44:36.8	0.60	98.15	1.00	WFI-R	20.56±0.01	18.81±0.03	0.522 ^a	2	0.52±0.01 ¹
201	3:32:52.08	-27:44:25.2	3:32:52.08	-27:44:25.1	0.10	146.99	1.00	WFI-R	20.78±0.01	18.49±0.03	0.534 ^b	2	0.46±0.02 ¹
202	3:32:52.54	-27:59:42.9											
203	3:32:52.91	-27:38:38.2	3:32:52.89	-27:38:38.0	0.20	31.42	0.99	WFI-R	23.57±0.04	>21.4	1.226 ^b	1	1.19±0.16 ¹
204	3:32:53.34	-28:01:59.6	3:32:53.34	-28:01:58.9	0.60	24.24	0.99	WFI-R	23.24±0.03	>21.4			1.13±0.01 ¹
205	3:32:54.70	-27:34:21.3	3:32:54.76	-27:34:21.4	0.90	124.67	1.00	WFI-R	18.35±0.01	>21.4			0.15±0.01 ¹
206	3:32:56.46	-27:58:47.3	3:32:56.45	-27:58:48.1	0.90	103.77	1.00	WFI-R	16.72±0.01	>21.4			0.15±0.01 ¹
207	3:32:57.08	-28:02:09.7	3:32:57.16	-28:02:09.9	1.20	30.49	0.99	WFI-R	20.37±0.01	>21.4			0.64±0.01 ¹
208	3:32:59.25	-27:48:58.2	3:32:59.31	-27:48:58.7	1.00	38.30	0.99	SOFI-K	23.37±0.03	20.31±0.09			1.28±0.98 ³
209	3:32:59.25	-27:43:24.2	3:32:59.21	-27:43:25.1	1.10	2.22	0.92	WFI-R	24.19±0.06	20.48±0.08			
210	3:32:59.30	-27:35:34.1	3:32:59.33	-27:35:34.1	0.50	33.83	0.99	WFI-R	22.63±0.02	>21.4	1.128 ^b	2	1.14±0.01 ¹
211	3:33:01.14	-27:58:16.1	3:33:01.12	-27:58:17.2	1.20	7.18	0.97	WFI-R	23.18±0.04	>21.4			
212	3:33:02.01	-27:49:54.0	3:33:02.08	-27:49:54.3	1.00	27.30	0.99	WFI-R	21.17±0.01	18.89±0.03	0.581 ^b	2	0.57±0.02 ¹
213	3:33:02.69	-27:56:41.4	3:33:02.62	-27:56:39.8	1.80	0.30	0.70	GEMS-z	>25.5	>21.4			
214	3:33:03.00	-27:51:46.0	3:33:03.05	-27:51:45.8	0.80	2.03	0.91	ACS-i	25.33±0.19	>24.7			3.69±0.57 ³
215	3:33:03.22	-27:53:06.1	3:33:03.18	-27:53:06.6	0.80	14.70	0.74	WFI-R	23.14±0.02	19.52±0.06			0.73±0.10 ¹
216	3:33:03.30	-27:53:28.0	3:33:03.31	-27:53:28.0	0.50	10.00	0.90	SPITZER	>25.5	>21.4			

Table 3—Continued

(1) RID	RADIO		OPTICAL		(6) dist (")	(7) LR	(8) Rel	(9) catalogue	(10) R (AB)	(11) K (AB)	(12) z	(13) Qual-z	(14) z_{phot}
	(2) RA (J2000)	(3) Dec	(4) RA (J2000)	(5) Dec									
217	3:33:03.73	-27:36:10.2	3:33:03.74	-27:36:11.0	0.90	58.46	1.00	WFI-R	20.17±0.01	>21.4	0.623 ^b	2	
218	3:33:03.87	-27:50:26.2	3:33:03.87	-27:50:26.2	0.10	34.86	0.99	WFI-R	21.99±0.01	19.44±0.04	0.890 ^e	2	0.86±0.05 ¹
219	3:33:04.50	-27:38:01.3	3:33:04.51	-27:38:02.5	1.30	2.33	0.92	WFI-R	23.58±0.04	>21.4	1.084 ^b	1	0.99±0.06 ¹
220	3:33:05.18	-27:40:26.1	3:33:05.14	-27:40:27.4	1.50	12.90	0.98	WFI-R	20.36±0.01	18.51±0.06			0.30±0.00 ¹
221	3:33:05.54	-27:54:15.0	3:33:05.53	-27:54:16.4	1.50	19.94	0.99	WFI-R	20.62±0.01	18.84±0.03	0.325 ^d	2	0.31±0.04 ¹
222	3:33:05.67	-27:33:28.9	3:33:05.67	-27:33:27.5	1.30	2.12	0.91	WFI-R	24.00±0.08	>21.4			
223	3:33:06.21	-27:48:42.0	3:33:06.16	-27:48:42.0	0.80	0.30	0.70	WFI-R	26.51±0.30	24.45±0.10			
224	3:33:06.85	-27:42:05.2	3:33:06.86	-27:42:05.5	0.50	40.36	1.00	WFI-R	21.78±0.01	18.66±0.04			0.56±0.04 ¹
225	3:33:07.32	-27:44:32.1	3:33:07.33	-27:44:32.6	0.70	228.79	1.00	WFI-R	17.66±0.01	16.29±0.01			0.21±0.02 ¹
226	3:33:07.51	-27:51:20.2	3:33:07.41	-27:51:21.0	1.50	0.10	0.33	WFI-R	25.96±0.39	>21.4			
227	3:33:07.75	-27:53:51.0	3:33:07.81	-27:53:50.9	1.00	6.20	0.80	WFI-R	23.74±0.05	21.20±0.40			
228	3:33:08.18	-27:50:33.0	3:33:08.17	-27:50:33.2	0.30	54.77	1.00	WFI-R	21.92±0.01	18.95±0.10	0.732 ^d	2	0.73±0.04 ¹
229	3:33:09.75	-27:48:01.1	3:33:09.74	-27:48:01.0	0.00	216.10	1.00	WFI-R	19.10±0.01	17.57±0.08	0.180 ^d	2	0.17±0.02 ¹
230	3:33:10.21	-27:48:42.1	3:33:10.20	-27:48:41.9	0.10	46.58	1.00	WFI-R	22.97±0.02	>21.4	1.029 ^d	2	0.81±0.06 ³
231	3:33:10.30	-27:33:06.0	3:33:10.31	-27:33:06.2	0.40	198.11	1.00	WFI-R	19.06±0.01	>21.4			
232	3:33:11.80	-27:41:37.9	3:33:11.79	-27:41:38.1	0.30	16.29	0.99	WFI-R	23.96±0.06	>21.4			1.06±0.12 ¹
233	3:33:11.90	-27:53:46.8	3:33:11.88	-27:53:46.8	0.20	163.42	1.00	WFI-R	20.33±0.01	>21.4	0.532 ^d	2	0.54±0.02 ¹
234	3:33:12.58	-27:53:22.0	3:33:12.60	-27:53:22.4	0.60	8.81	0.98	WFI-R	24.19±0.08	>21.4			
235	3:33:13.15	-27:49:30.9	3:33:13.11	-27:49:30.4	0.50	38.86	0.99	SOFI-K	>25.5	>21.4			
236	3:33:14.50	-27:47:47.9	3:33:14.52	-27:47:47.6	0.40	12.92	0.98	WFI-R	24.02±0.05	>21.4			
237	3:33:14.85	-28:04:31.8	3:33:15.03	-28:04:29.4	3.40	0.01	0.01	WFI-R	23.59±0.05	>21.4			
238	3:33:14.98	-27:51:50.9	3:33:14.99	-27:51:51.1	0.30	37.59	0.99	WFI-R	23.19±0.03	>21.4	1.998 ^d	1	1.10±0.06 ¹
239	3:33:16.37	-27:47:25.0	3:33:16.35	-27:47:24.8	0.20	43.48	1.00	WFI-R	22.94±0.02	>21.4			1.03±0.02 ¹
240	3:33:16.49	-27:50:39.8	3:33:16.52	-27:50:39.5	0.50	232.28	1.00	WFI-R	17.44±0.01	>21.4	0.086 ^d	2	0.09±0.04 ¹
241	3:33:16.75	-27:56:29.8	3:33:16.75	-27:56:30.0	0.30	111.95	1.00	WFI-R	21.11±0.01	>21.4			0.57±0.02 ¹
242	3:33:16.78	-28:00:15.9	3:33:16.77	-28:00:16.4	0.60	1.21	0.86	WFI-R	25.53±0.18	>21.4			
243	3:33:16.94	-27:41:20.9	3:33:16.94	-27:41:21.5	0.70	199.26	1.00	WFI-R	18.03±0.01	>21.4	0.148 ^b	2	0.14±0.01 ¹
244	3:33:17.38	-27:49:48.8	3:33:17.44	-27:49:47.1	1.80	0.01	0.05	WFI-R	25.47±0.13	>21.4			
245	3:33:17.75	-27:49:42.8	3:33:17.84	-27:49:44.8	2.40	0.01	0.01	WFI-R	24.81±0.07	>21.4			
246	3:33:17.76	-27:59:06.8	3:33:17.77	-27:59:06.2	0.60	29.44	0.99	WFI-R	22.74±0.02	>21.4			1.13±0.03 ¹
247	3:33:18.32	-27:34:40.6	3:33:18.29	-27:34:39.8	0.80	0.89	0.82	WFI-R	25.36±0.09	>21.4			

Table 3—Continued

(1) RID	RADIO		OPTICAL		(6) dist (")	(7) LR	(8) Rel	(9) catalogue	(10) R (AB)	(11) K (AB)	(12) z	(13) Qual-z	(14) z_{phot}
	(2) RA (J2000)	(3) Dec	(4) RA (J2000)	(5) Dec									
248	3:33:18.73	-27:49:40.7	3:33:18.71	-27:49:39.8	0.80	7.63	0.97	WFI-R	23.98±0.05	>21.4			
249	3:33:19.06	-27:35:31.0	3:33:19.04	-27:35:30.9	0.20	287.32	1.00	WFI-R	18.11±0.01	>21.4			0.14±0.01 ¹
250	3:33:20.61	-27:49:10.2	3:33:20.60	-27:49:10.1	0.00	129.55	1.00	WFI-R	16.26±0.01	>21.4	0.126 ^d	2	0.14±0.00 ¹
251	3:33:20.93	-27:47:56.4	3:33:20.86	-27:47:55.4	1.20	17.21	0.97	WFI-R	16.23±0.01	>21.4	0.129 ^b	2	0.14±0.00 ¹
252	3:33:21.31	-27:41:37.8	3:33:21.32	-27:41:38.4	0.80	15.61	0.99	WFI-R	23.40±0.06	>21.4			1.15±0.15 ¹
253	3:33:25.85	-27:43:42.7	3:33:25.85	-27:43:42.5	0.10	148.17	1.00	WFI-R	20.59±0.01	>21.4	0.537 ^b	2	0.57±0.00 ¹
254	3:33:26.54	-27:44:44.7	3:33:26.51	-27:44:44.8	0.30	134.54	1.00	WFI-R	20.20±0.01	>21.4	0.448 ^b	2	0.44±0.01 ¹
255	3:33:27.55	-27:57:25.6	3:33:27.54	-27:57:25.8	0.30	3.40	0.94	WFI-R	25.11±0.14	>21.4			
256	3:33:30.73	-27:44:02.6	3:33:30.69	-27:44:02.9	0.60	24.91	0.99	WFI-R	22.71±0.02	>21.4	0.864 ^b	2	0.77±0.02 ¹
257	3:33:32.61	-27:35:39.5	3:33:32.57	-27:35:38.5	1.00	46.94	1.00	WFI-R	19.81±0.01	>21.4			0.56±0.01 ¹
258	3:33:33.46	-27:53:32.5	3:33:33.42	-27:53:32.6	0.40	87.05	1.00	SOFI-K	>25.5	>21.4			
259	3:33:34.55	-27:47:51.4	3:33:34.56	-27:47:51.0	0.40	32.55	0.99	WFI-R	22.91±0.02	>21.4	0.860 ^b	2	0.63±0.03 ¹
260	3:33:35.35	-27:45:49.4	3:33:35.19	-27:45:50.0	2.10	3.51	0.95	WFI-R	17.42±0.01	>21.4			0.20±0.01 ¹
261	3:33:36.31	-27:44:32.3	3:33:36.34	-27:44:31.9	0.50	6.70	0.97	WFI-R	24.42±0.07	>21.4			
262	3:33:36.45	-27:43:55.5	3:33:36.48	-27:43:56.5	1.20	0.45	0.45	WFI-R	25.22±0.12	>21.4			
263	3:33:36.85	-27:36:40.4	3:33:36.88	-27:36:40.5	0.60	6.65	0.97	WFI-R	24.30±0.09	>21.4	3.678 ^b	1	
264	3:33:38.38	-28:00:31.2	3:33:38.32	-28:00:30.4	1.00	37.09	0.99	WFI-R	20.85±0.01	>21.4			
265	3:33:41.30	-27:38:08.4	3:33:41.29	-27:38:08.4	0.10	389.68	1.00	WFI-R	17.41±0.01	>21.4	0.102 ^b	2	
266	3:33:42.38	-27:47:37.2	3:33:42.36	-27:47:36.9	0.30	39.05	0.99	WFI-R	22.95±0.03	>21.4	0.776 ^b	2	

^aSpectroscopic redshift from Szokoly et al. (2004). The average redshift uncertainty is $\Delta z=0.005$.

^bSpectroscopic redshift from Silvermann et al., in preparation.

^cSpectroscopic redshift from Vanzella et al. 2005, 2006, 2008. The average redshift uncertainty is $\Delta z=0.00055$.

^dSpectroscopic redshift from Popesso et al. (2008).

^eSpectroscopic redshift from Le Fevre et al. (2004). The average redshift uncertainty is $\Delta z=0.0012$.

^fSpectroscopic redshift from Mignoli et al. (2005).

^gSpectroscopic redshift from Ravikumar et al. (2007).

¹Photometric redshift from Wolf et al. (2004).

²Photometric redshift from Grazian et al. (2006).

³Photometric redshift from Zheng et al. (2004).

*The optical photometry could be contaminated by a close-by bright star.

*The optical photometry could be contaminated by a close-by (≈ 1.3 arcsec) source.

Table 4. Optical, near infrared secondary counterparts of the 20 cm sources in the E-CDF-S

(1) RID	RADIO		OPTICAL		(6) dist (")	(7) LR	(8) Rel	(9) catalogue	(10) R (AB)	(11) K (AB)	(12) z	(13) Qual-z	(14) z_{phot}
	(2) RA (J2000)	(3) Dec	(4) RA (J2000)	(5) Dec									
38	3:31:44.48	-27:42:11.0	3:31:44.49	-27:42:10.0	1.00	0.74	0.11	WFI-R	25.15±0.10	>21.4			
71	3:32:00.84	-27:35:56.4	3:32:00.91	-27:35:55.4	1.40	1.00	0.03	WFI-R	24.23±0.04	>21.4			0.88±0.06 ¹
98	3:32:13.19	-27:57:44.4	3:32:13.25	-27:57:43.7	1.10	1.13	0.12	WFI-R	24.77±0.05	>21.4			
101	3:32:13.52	-27:49:52.5	3:32:13.46	-27:49:51.9	0.80	13.81	0.18	ACS-i	22.78±0.02	19.80±0.01	0.731 ^c	2	0.69±0.08 ²
110	3:32:17.22	-27:52:21.3	3:32:17.27	-27:52:19.6	1.70	0.75	0.01	ACS-i	24.48±0.04	22.00±0.04	1.097 ^a	2	0.34±0.08 ²
113	3:32:19.17	-27:54:07.7	3:32:19.11	-27:54:07.2	0.60	44.02	0.99	ACS-i	24.08±0.03	20.40±0.01	0.964 ^a	2	0.98±0.08 ²
118	3:32:21.00	-27:47:06.3	3:32:21.05	-27:47:07.3	1.50	8.26	0.09	ACS-i	23.08±0.01	21.34±0.03			0.62±0.08 ²
120	3:32:21.29	-27:44:35.6	3:32:21.32	-27:44:36.4	1.10	71.01	0.14	ACS-i	20.53±0.01	18.22±0.01	0.524 ^b	2	0.49±0.08 ²
121	3:32:22.04	-27:42:44.0	3:32:22.16	-27:42:43.8	1.70	1.94	0.14	ACS-i	24.15±0.04	22.38±0.07	1.877 ^d	1	1.78±0.08 ²
121	3:32:22.04	-27:42:44.0	3:32:22.05	-27:42:41.9	2.00	0.70	0.05	ACS-i	24.98±0.07	>24.7			0.66±0.08 ²
126	3:32:22.68	-27:41:26.1	3:32:22.85	-27:41:24.8	2.60	0.62	0.03	ISAAC-K	24.70±0.10	21.78±0.04			2.02±0.08 ²
136	3:32:27.97	-27:46:39.4	3:32:28.00	-27:46:37.7	1.60	2.21	0.00	ACS-i	22.72±0.01	22.08±0.01			0.04±0.08 ²
145	3:32:31.47	-27:46:23.3	3:32:31.41	-27:46:21.4	1.90	0.51	0.01	ACS-i	23.89±0.03	23.01±0.09	2.223 ^a	2	0.75±0.08 ²
160	3:32:37.29	-27:51:27.4	3:32:37.17	-27:51:27.9	1.50	17.19	0.19	ACS-i	22.48±0.01	19.58±0.01			1.01±0.08 ²
161	3:32:37.79	-27:50:00.4	3:32:37.76	-27:50:01.4	1.10	6.68	0.23	ACS-i	23.95±0.05	21.83±0.03	1.004 ^c	1	1.00±0.08 ²
162	3:32:37.80	-27:52:12.4	3:32:37.92	-27:52:11.8	1.90	0.37	0.01	ACS-i	24.18±0.05	>24.7	1.603 ^a	2	0.69±0.08 ²
164	3:32:38.80	-27:44:49.2	3:32:38.66	-27:44:49.2	1.70	0.26	0.00	ACS-i	26.30±0.10	>24.7			0.06±0.08 ²
169	3:32:39.47	-27:53:01.3	3:32:39.47	-27:53:00.5	0.70	197.29	0.46	ACS-i	21.25±0.01	19.15±0.01			0.68±0.08 ²
170	3:32:39.68	-27:48:51.4	3:32:39.55	-27:48:51.7	1.60	1.95	0.13	ACS-i	24.84±0.06	21.81±0.03	3.064 ^a	2	3.06±0.08 ²
177	3:32:43.16	-27:55:14.3	3:32:43.26	-27:55:15.1	1.80	0.28	0.01	ACS-i	23.83±0.05	21.44±0.31	0.579 ^d	2	
192	3:32:48.59	-27:49:34.4	3:32:48.51	-27:49:34.9	1.10	0.99	0.04	ACS-i	24.64±0.11	21.09±0.02	1.117 ^e	2	1.11±0.08 ²
215	3:33:03.22	-27:53:06.1	3:33:03.29	-27:53:06.7	1.20	5.06	0.25	WFI-R	23.65±0.02	20.06±0.06			0.82±0.06 ¹
227	3:33:07.75	-27:53:51.0	3:33:07.70	-27:53:50.2	0.90	1.32	0.17	WFI-R	24.87±0.07	>21.4			
251	3:33:20.93	-27:47:56.4	3:33:21.20	-27:47:53.1	4.90	0.29	0.02	WFI-R	21.66±0.01	>21.4			
262	3:33:36.45	-27:43:55.5	3:33:36.37	-27:43:53.9	1.80	0.35	0.35	WFI-R	23.92±0.05	>21.4			1.11±0.09 ¹

^aSpectroscopic redshift from Szokoly et al. (2004). The average redshift uncertainty is $\Delta z=0.005$.

^bSpectroscopic redshift from Silvermann et al., in preparation.

^cSpectroscopic redshift from Vanzella et al. 2005, 2006, 2008. The average redshift uncertainty is $\Delta z=0.00055$.

^dSpectroscopic redshift from Popesso et al. (2008)

^eSpectroscopic redshift from Le Fevre et al. (2004). The average redshift uncertainty is $\Delta z=0.0012$.

^fSpectroscopic redshift from Mignoli et al. (2005).

¹Photometric redshift from Wolf et al. (2004).

²Photometric redshift from Grazian et al. (2006).

³Photometric redshift from Zheng et al. (2004).

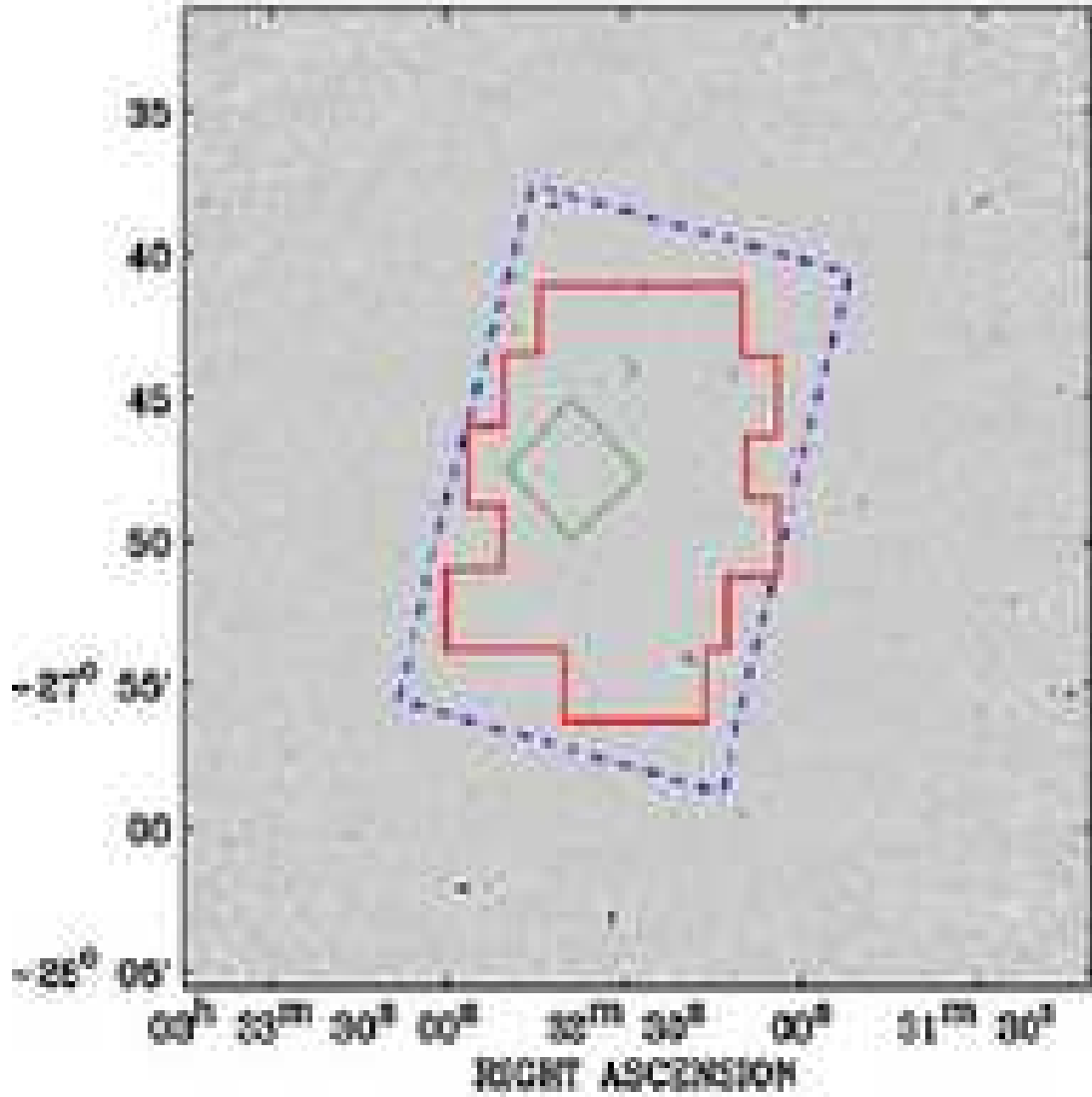


Fig. 1.— Multiwavelength coverage of the VLA/CDF-S Survey. The background image is the 20 cm VLA observation. The area covered by ACS as part of the GOODS program is highlighted with a dashed line; the continuous line shows the overlay of the ISAAC/VLT deep Ks band imaging and finally the location of the UDF is indicated by the small square in the center.

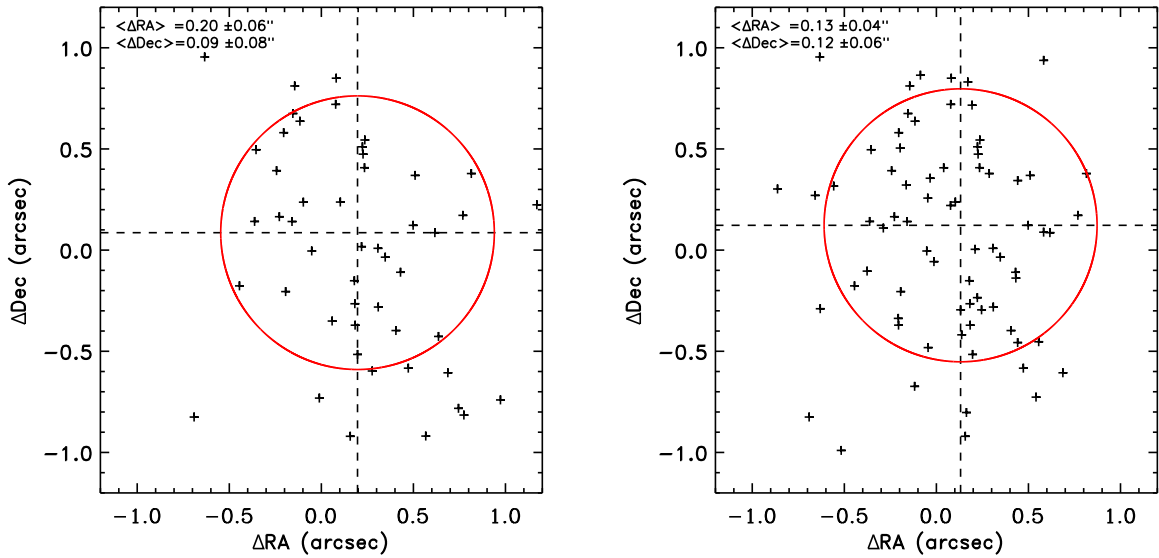


Fig. 2.— Offsets between the radio and the WFI-R (left panel) and SOFI-Ks (right panel) coordinates. We used only radio point-like sources with $S/N > 5$ associated with a point-like counterpart. The circle is centered on the average offset found and its radius is equal to the average uncertainty in the radio coordinates.

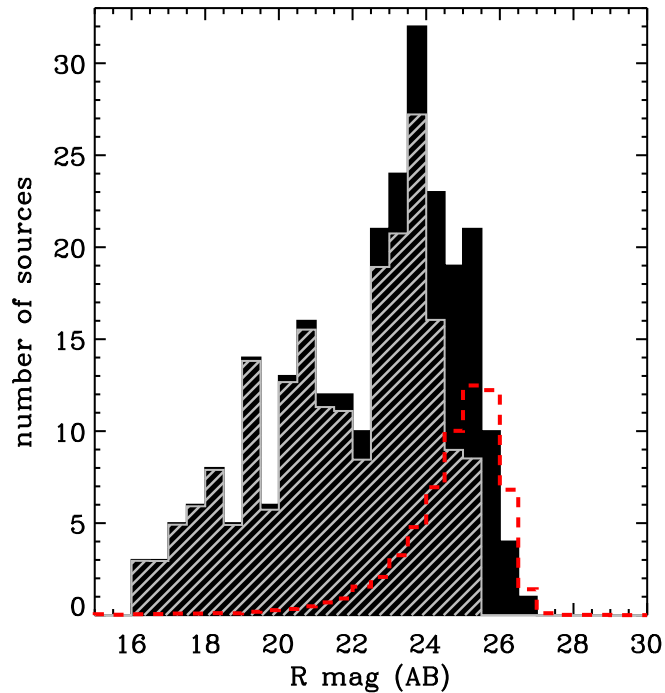


Fig. 3.— The different component of Eq. (1) for the WFI-R catalogue. Magnitude distribution of possible counterparts found in circles of 2 arcsec radius around the radio sources (black filled histogram). The dashed histogram is the magnitude distribution of background objects that we expect to have in the area where the search for counterparts is performed (equal to the surface density as a function of magnitude of background objects, $n(m)$, times the area of a circle of 2 arcsec radius times the number of radio sources). Finally, the magnitude distribution of optical counterparts once the background objects have been subtracted (grey hatched histogram).

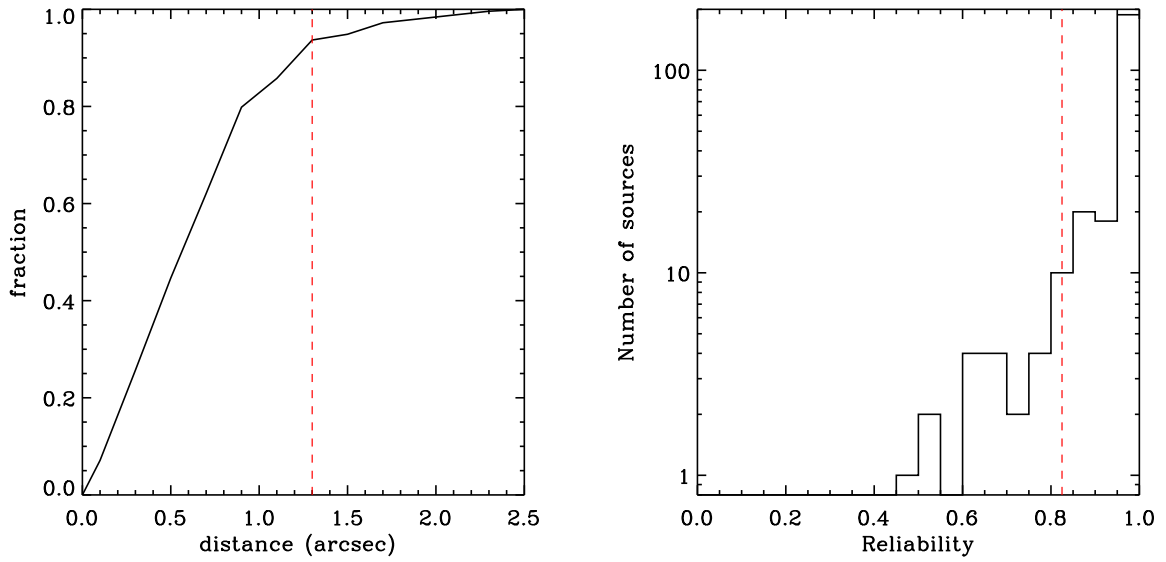


Fig. 4.— *Left*: the cumulative distribution of the radio to optical/NIR separations. The dashed line indicates a separation of $1.3''$ within which 90% of the counterparts are located. *Right*: the distribution of the reliability parameter, R , for the radio counterparts. The dashed line at $R=0.83$ marks the reliability value above which 90% of the counterparts are located.

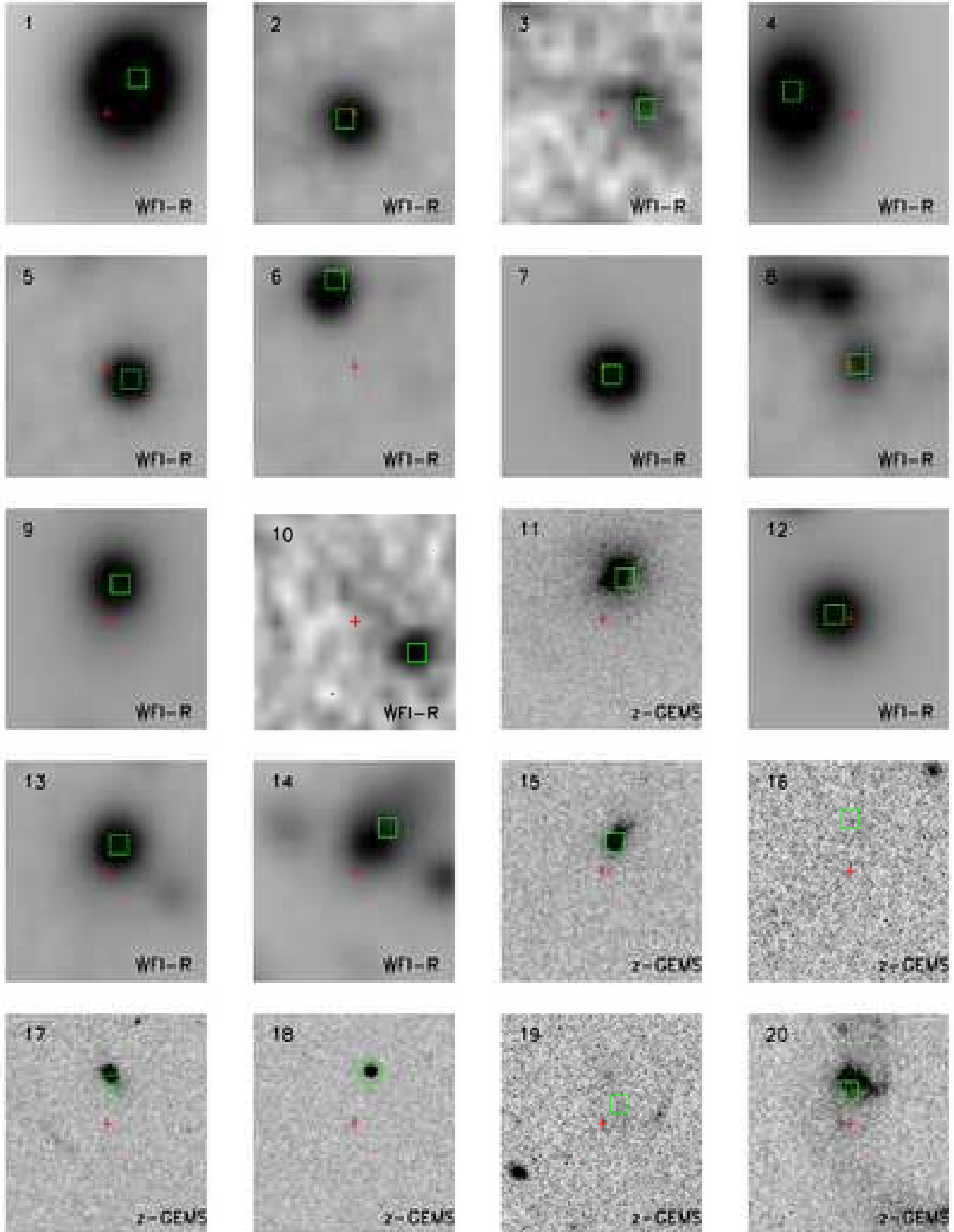


Fig. 5.— Cutouts of the radio sources either from ACS (GOODS-i, GEMS-z) or WFI-R. Each one is 5 arcsec on a side. The red cross indicates the radio position, the green square the primary counterpart while the blue triangles are possible secondary counterparts. The complete series of cutouts is available in the electronic version of the paper.

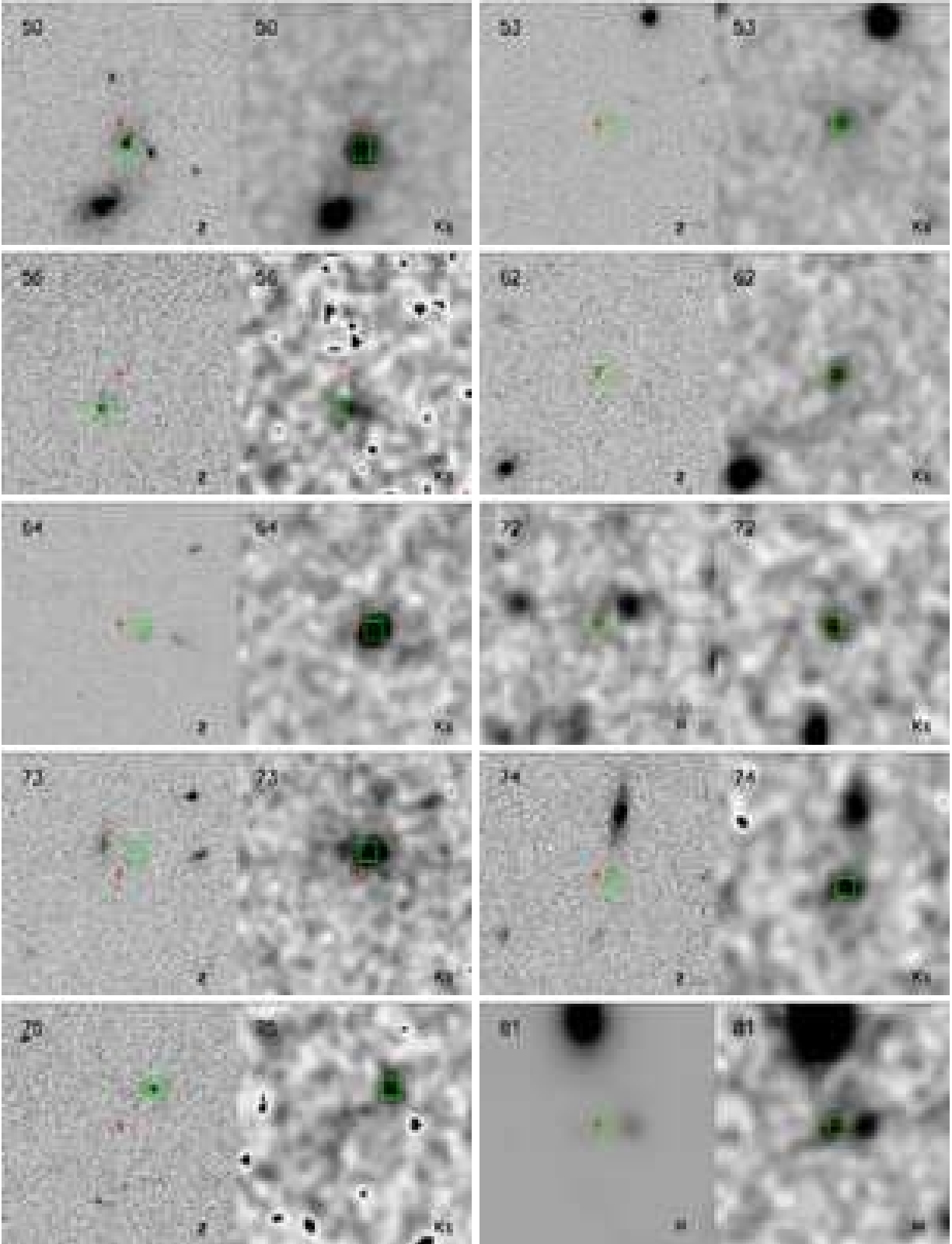


Fig. 6.— Cutouts of the radio sources identified in the K band. For each of these sources, we show the optical (left) and K band(right) cutouts. Each one is 10 arcsec on a side. The red cross indicated the radio position, the green square the primary counterpart while the blue triangles are possible secondary counterparts.

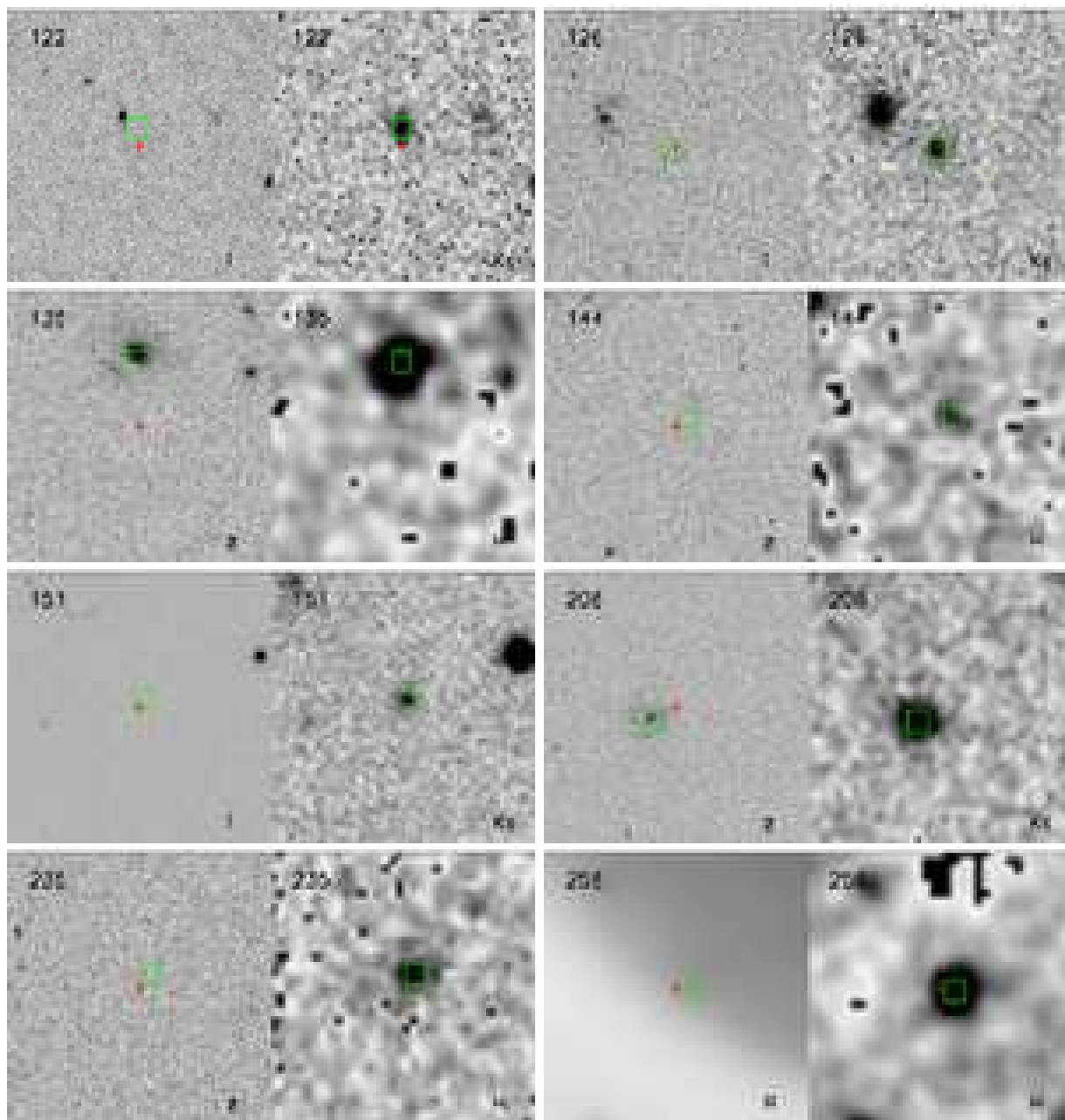


Fig. 6. — Continued.

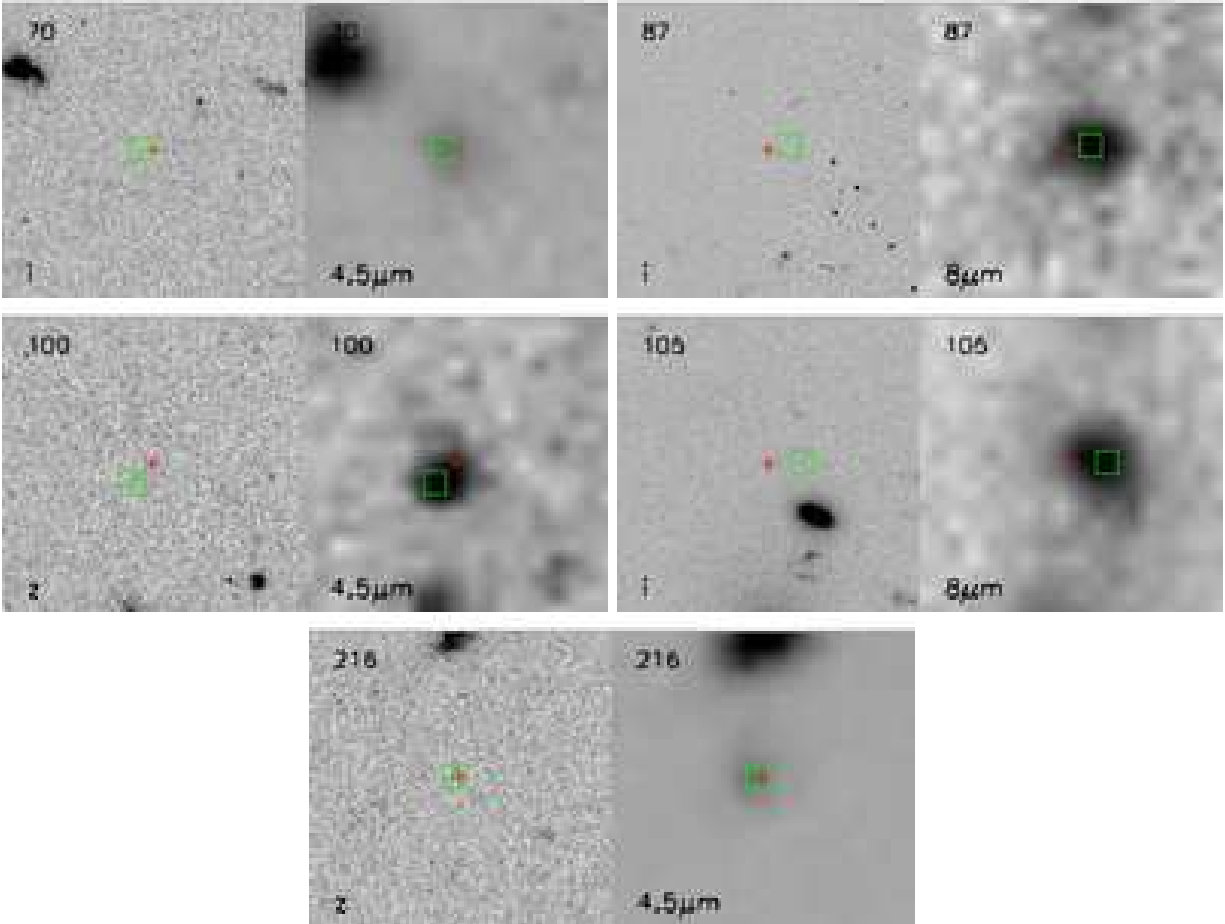


Fig. 7.— Cutouts of the radio sources identified in the Spitzer bands. For each of these sources, we show the optical (left) and IR (right) cutouts. Each one is 10 arcsec on a side. The red cross indicated the radio position, the green square the primary counterparts while the blue triangles are possible secondary counterparts.

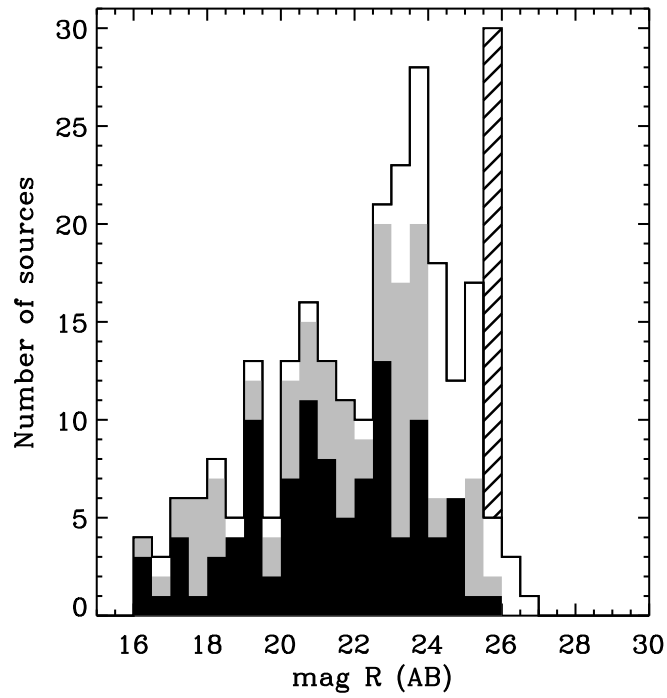


Fig. 8.— R magnitudes distribution for the primary counterparts (the total histogram). Black shading refers to sources with spectroscopic redshifts, the grey shading denotes objects with photometric redshifts and finally radio sources with no counterparts in the R band and for which we can only provide lower limit to their magnitudes are represented by the hatched box.

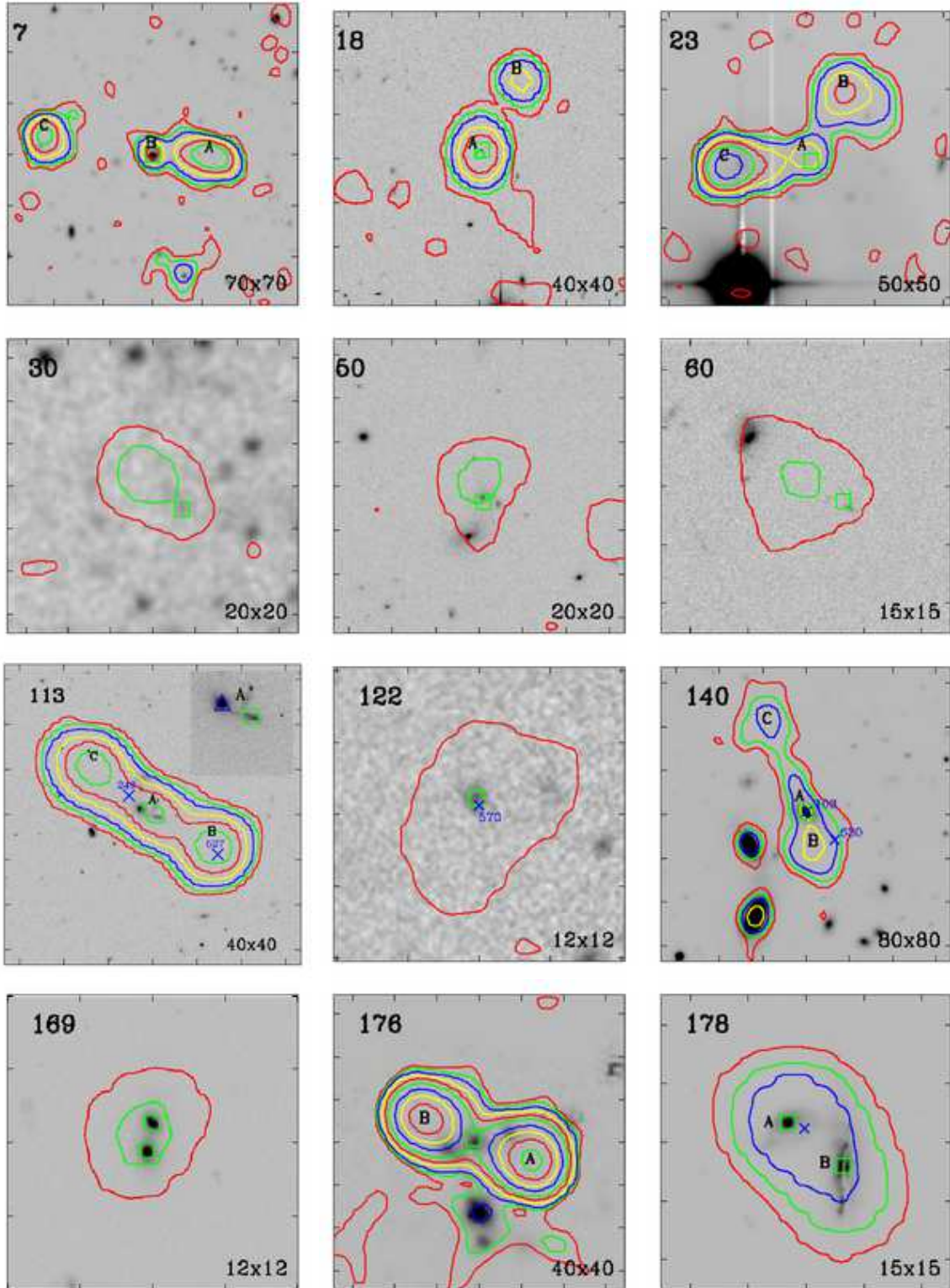


Fig. 9.— Cutouts of some particular radio source discussed in Section 5 with overlaid radio contours. The green square indicates the primary counterpart while the blue x are X-ray detections. The id of the source is on the top-left corner, while the dimension (in arcsec) of the cutout is reported on the bottom-right corner.

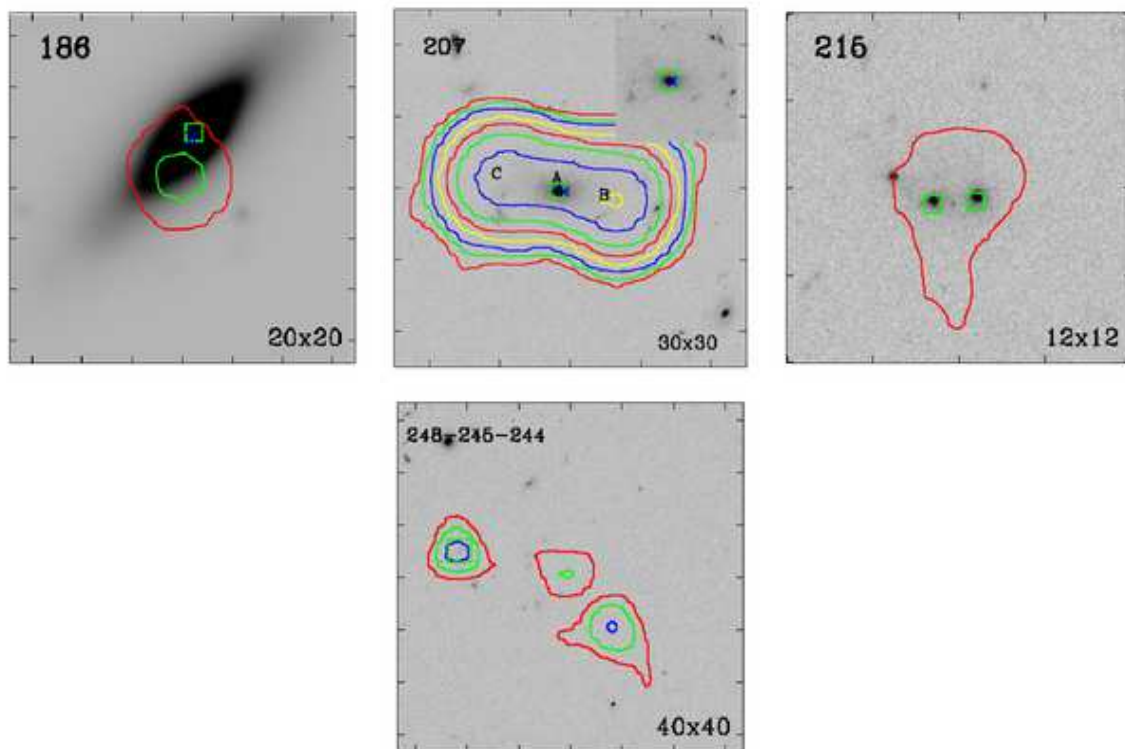


Fig. 9. — Continued.

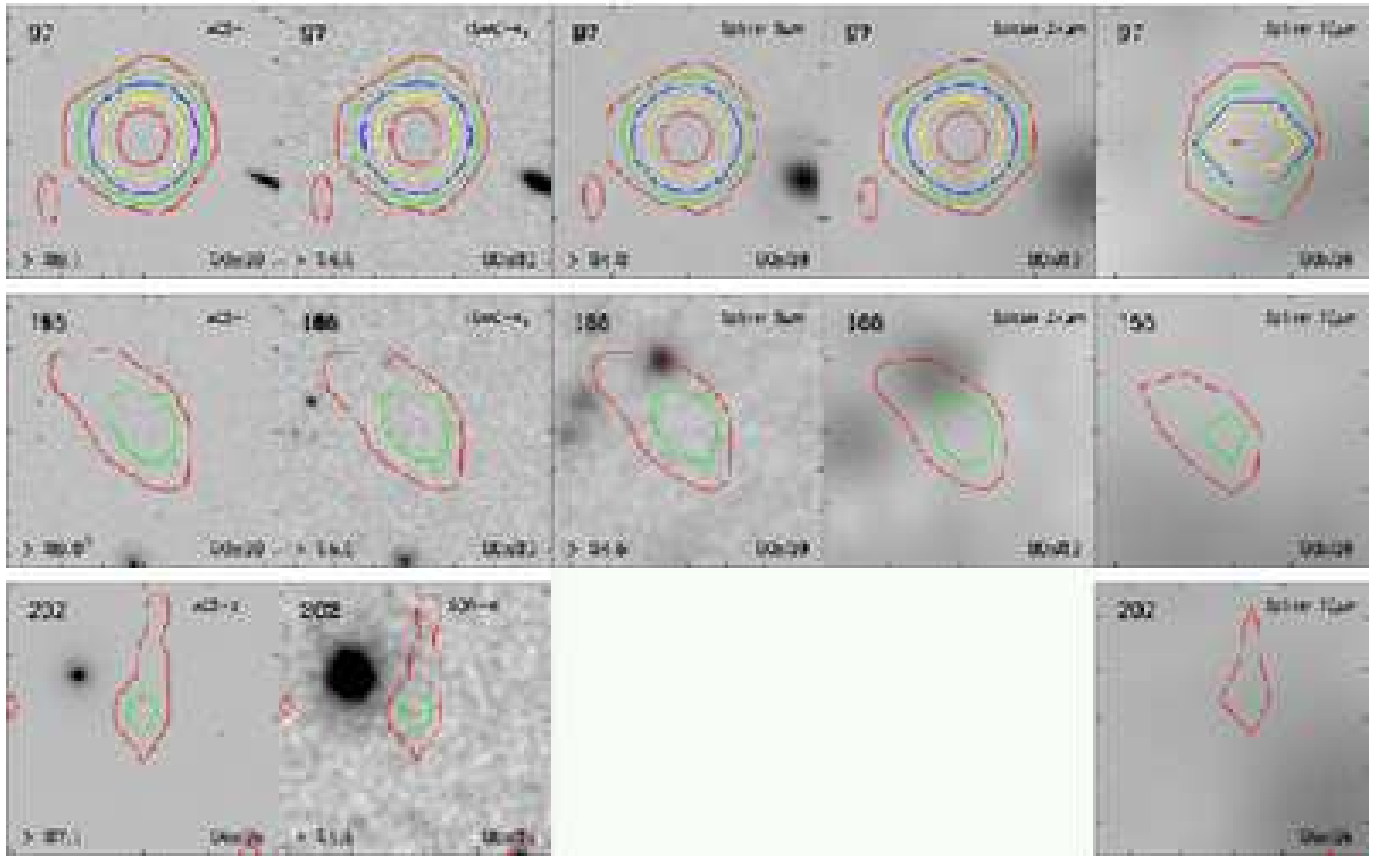


Fig. 10.— Cutouts of the three sources without any counterpart. In each cutout is indicated the sources identification number (top-left), the band (top-right), the 1σ magnitude limit (bottom-left) and the dimensions of the cutout (bottom-right).

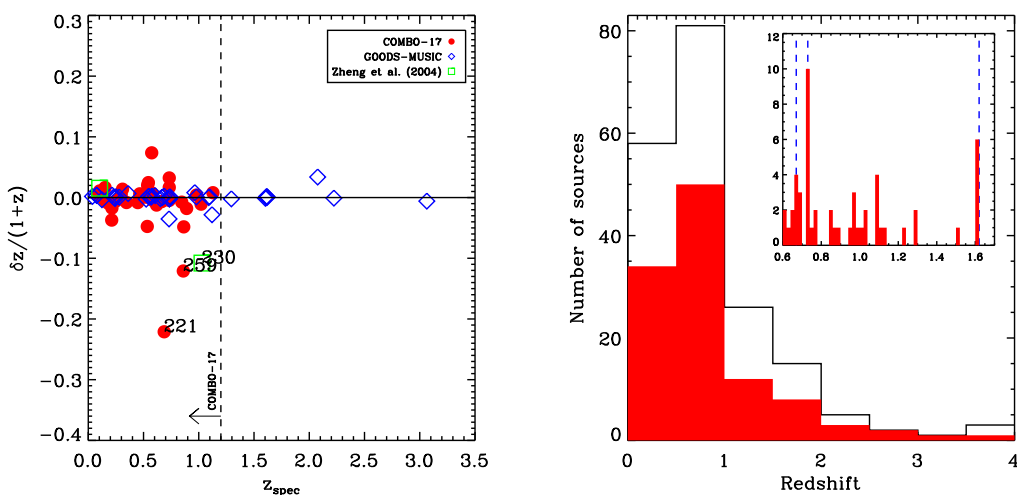


Fig. 11.— *Left*: Photometric redshift errors as a function of redshift. The dashed line indicates the value of $z=1.2$ to which we limit our use of this dataset. *Right*: Redshift distribution for the VLA/CDF-S sample. The total histogram is obtained using both spectroscopic (49) and photometric (110) redshifts, while the shaded one refers only to the spectroscopic one. The inset is a zoom in the region $0.6 < z < 1.7$ with a redshift bin of 0.02. The vertical dashed lines shows the location of three redshift spikes reported by Gilli et al. (2003) at $z=0.67, 0.73, 1.61$.

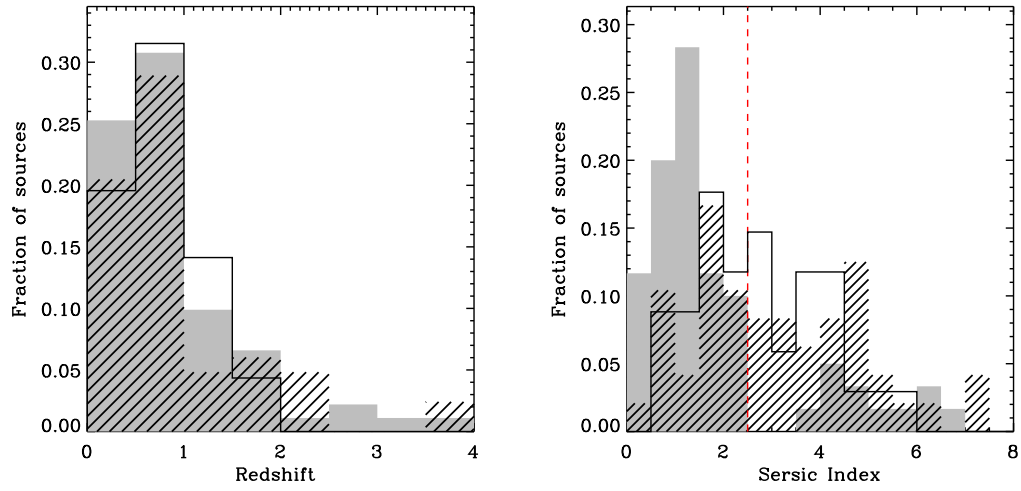


Fig. 12.— Left panel: redshift distribution for radio sources with $S(1.4 \text{ GHz}) > 0.2 \text{ mJy}$ (continuous line), $0.08 < S(1.4 \text{ GHz}) < 0.2$ (hatched histogram) and $S(1.4 \text{ GHz}) < 0.08 \text{ mJy}$ (grey shaded histogram). Right panel: distribution of the Sersic index values for radio sources with $S(1.4 \text{ GHz}) > 0.2 \text{ mJy}$ (continuous line), $0.08 < S(1.4 \text{ GHz}) < 0.2$ (hatched histogram) and $S(1.4 \text{ GHz}) < 0.08 \text{ mJy}$ (grey shaded histogram). The vertical line mark the value $n = 2.5$, empirical dividing value between early and late type galaxies.

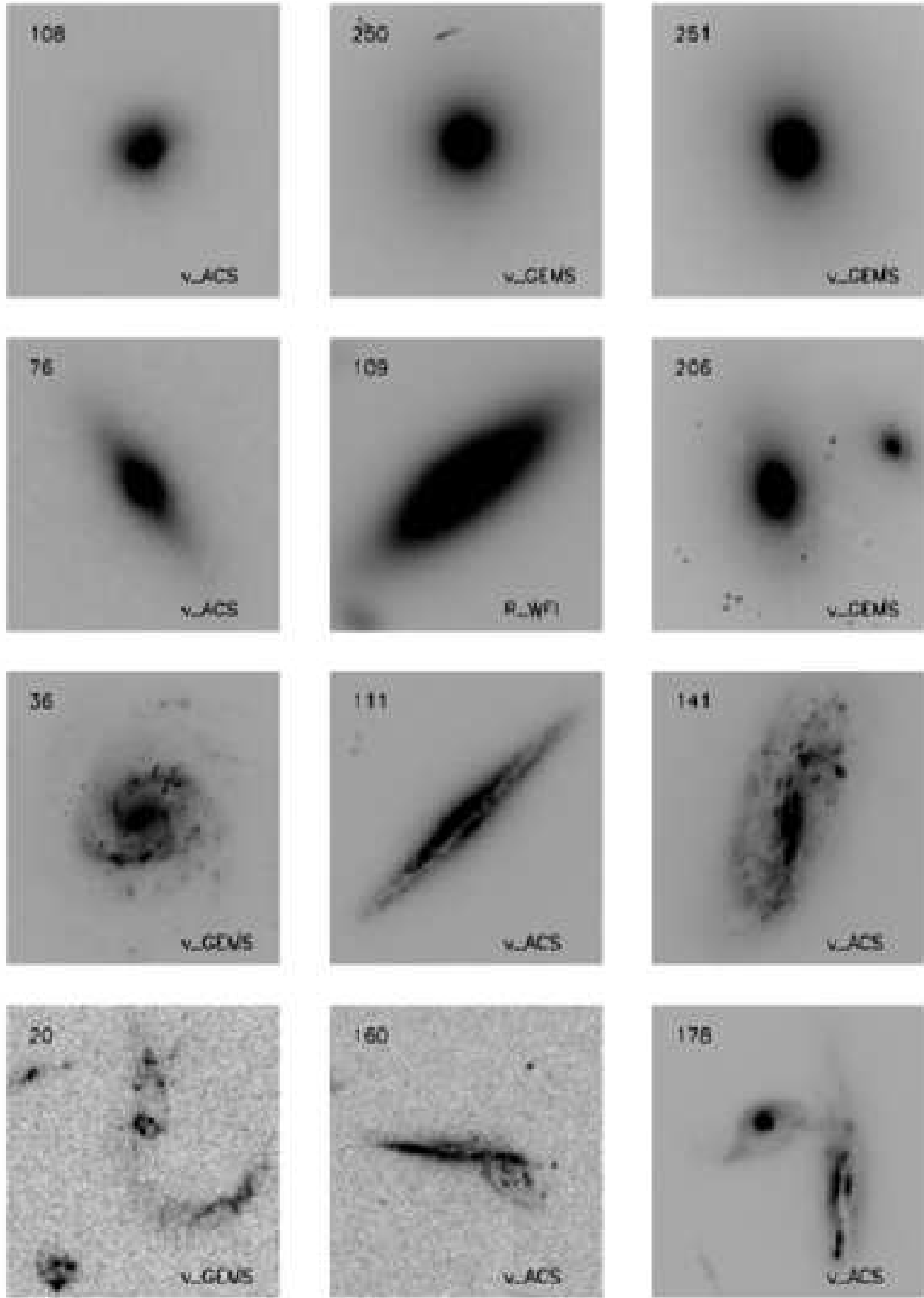


Fig. 13.— Image cutouts ($10'' \times 10''$) of sources belonging to the four morphological classes defined in Sec. 7: E (first row), S0 (second row), S (third row), I (fourth row).

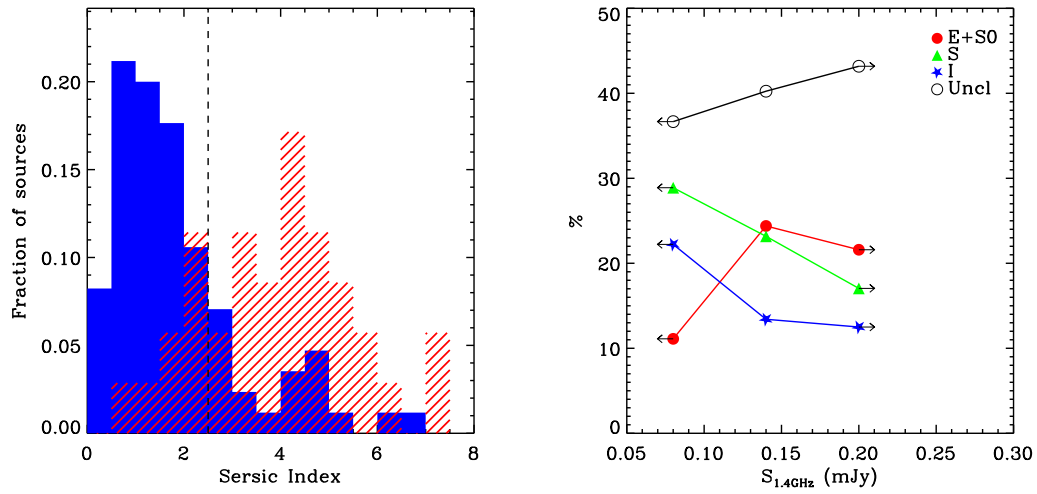


Fig. 14.— Left panel: distribution of Sersic index values for sources with visual morphological classification 'E' or 'S0' (hatched histogram) and 'S' or 'I' (shaded histogram). Right panel: percentages of E+S0, S, I and unclassified sources in the three radio flux density intervals defined in Sec. 7.

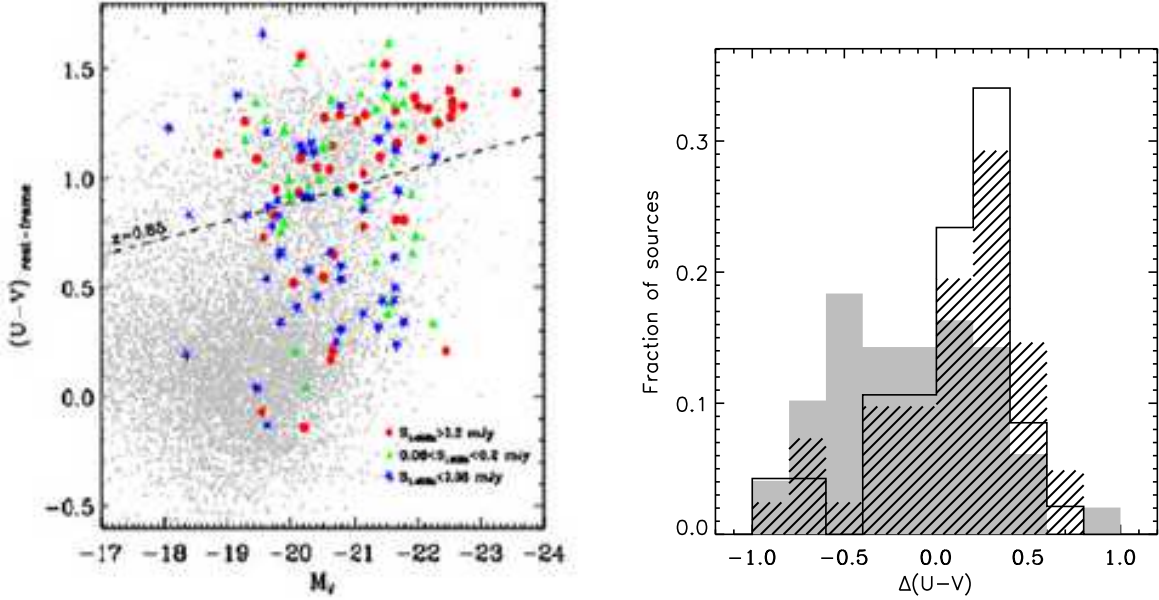


Fig. 15.— *Left panel:* Rest-frame U-V colors versus the absolute magnitude in the V band for radio sources with $S > 0.2$ mJy (circles), $0.08 < S < 0.2$ mJy (triangles), $S < 0.08$ mJy (stars) and optically selected galaxies from COMBO-17 (grey dots). The dashed line is the lower edge of red-sequence galaxies as defined by Bell et al. (2004) with $z=0.85$ (average redshift of our radio sources). *Right panel:* distribution of the difference between the rest-frame U-V color and the value of the lower edge of red-sequence galaxies (see left panel) for a given M_V value. The continuous line refers to radio sources with $S > 0.2$ mJy, the hatched histogram to $0.08 < S < 0.2$ mJy and finally sources with $S < 0.08$ mJy are represented by the shaded histogram.